Florian Franz Erich Borsodi BSc

Implementation and Evaluation of a Probabilistic Diffusion Tractography Method for Regional Assessment of the Brain

MASTER'S THESIS

to achieve the university degree of

Diplom-Ingenieur

Master's degree programme: Biomedical Engineering

submitted to

Graz University of Technology

Supervisor

Univ.-Prof. Dipl.-Ing. Dr.techn. Rudolf Stollberger

Institute of Medical Engineering

Graz, Oktober 23, 2018

AFFIDAVIT

I declare that I have authored this thesis independently, that I have not used other than the declared sources/resources, and that I have explicitly indicated all material which has been quoted either literally or by content from the sources used. The text document uploaded to TUGRAZonline is identical to the present master‘s thesis.

23.10.2018
Date

Borsotti
Signature

Titel

Implementierung und Evaluierung einer probabilistischen Methode zur regionalen Traktografie des menschlichen Gehirns

Kurzfassung

Diffusions-Tensor-Bildgebung ist eine quantitative Magnetresonanztomografiemethode zur Untersuchung der anisotropen Diffusionseigenschaften von weißer Substanz im Gehirn. Aus diesen Diffusions-Tensoren lassen sich Fasertrakte generieren welche die Nervenfaserbündel im Gehirn nichtinvasiv darstellen. Jedoch sind die meisten Methoden zur Diffusions-Tensor-Bildgebung und Traktografie zeitintensiv und verlangen die Interaktion einer Person. Daher wurde im Rahmen dieser Arbeit das Traktografieverfahren TRACULA implementiert, welches die automatische Identifizierung und Rekonstruktion von 18 Faserbündel erlaubt, und anhand der Resultate von 213 gesunden Probanden und 27 Patienten evaluiert. Die Faserbündelrekonstruktionen und traktspezische Diffusionseigenschaften, von gesunden Probanden, zeigten Änderungen aufgrund von Bildauflösung, Anzahl an Diffusionsrichtungen und Alter. In Patienten mit Amyotropher Lateralsklerose wurde eine Erhöhung von mittlerer und radialer Diffusivität in bilateralen corticospinalen Trakten festgestellt. Des Weiteren nahm die fraktionelle Anisotropie im corticospinalem Trakt und im Superior Longitudinal Fasciculus parietal beidseitig ab. Diese Resultate sind in Übereinstimmung mit der vorherrschenden Literatur und unterstreichen die Stabilität und Zuverlässigkeit von TRACULA, als auch dessen Potential zur klinischen Anwendung.

Schlüsselwörter

MRI, Diffusion, Diffusions-Tensor-Bildgebung, Traktografie, Gehirn

Title

Implementation and Evaluation of a Probabilistic Diffusion Tractography Method for Regional Assessment of the Brain

Abstract

Diffusion tensor imaging is a quantitative magnetic resonance imaging method, which probes the anisotropic diffusion properties of white matter in the brain. Furthermore, it is possible to generate fiber tracts from these diffusion tensors, which are non-invasive visual representations of nerve fiber bundles. However, most methods for diffusion tensor imaging and tractography are time consuming and require extensive user interaction. Therefore, this thesis demonstrates the implementation of TRACULA, a technique for the automatic identification and reconstruction of 18 fiber tracts, and its evaluation based on results from 213 healthy probands and 27 Patients. Changes in tract reconstructions and tract-specific diffusion properties were found for healthy subjects, regarding image resolution, number of diffusion directions and age. Amyotrophic lateral sclerosis patients showed an increase in mean and radial diffusivity for bilateral corticospinal tracts. Furthermore, fractional anisotropy was decreased for ambilateral corticospinal tracts and superior longitudinal fasciculus parietal. These results are in agreement with the literature and emphasize the stability and reliability of TRACULA, as well as its potential in clinical use.

Keywords

MRI, Diffusion, Diffusion Tensor Imaging, Tractography, Brain

Table of Contents

Acknowledgements ... **III**

Acronyms and Abbreviations ... **IV**

List of Figures ... **VI**

List of Tables ... **IX**

1 Introduction ... **1**

2 Theory ... **3**

- 2.1 Diffusion Principles ... 3
- 2.2 dMRI Measurement ... 5
- 2.3 DWI ... 8
- 2.4 DTI ... 9
- 2.5 Higher Order Diffusion Models ... 13
- 2.6 Fiber Tractography ... 14
- 2.7 Stroke ... 16
- 2.8 ALS ... 17

3 Methods ... **18**

- 3.1 Subjects ... 18
- 3.2 Data acquisition ... 19
  - 3.2.1 Multiresolution dataset ... 19
  - 3.2.2 Normal Healthy Subjects ... 19
  - 3.2.3 ALS ... 20
- 3.3 Software implementation ... 20
- 3.4 Image analysis ... 20
  - 3.4.1 Preprocessing ... 20
  - 3.4.2 DTI and Fiber Tractography ... 21
  - 3.4.3 Postprocessing ... 27
- 3.5 Statistical analysis ... 27

4 Results ... **28**

- 4.1 Multiresolution dataset ... 28
- 4.2 Normal Healthy Subjects ... 38
- 4.3 ALS ... 43

5 Discussion 45
5.1 Software 45
5.2 Multiresolution dataset 47
5.3 Normal Healthy Subjects 48
5.4 ALS 48
5.5 Statistical Analysis 48
5.6 Conclusion 49

References 50

Acknowledgements

Ich möchte mich bei meinen Eltern, Petra und Karl-Heinz, und bei meinen Großeltern, Susanne und Erich, für ihre uneingeschränkte Unterstützung und moralischen Beistand bedanken.
Des Weiteren möchte ich mich bei Teila für ihre Geduld und Beistand bedanken.
Vielen Dank auch an meine Freunde Julia, Samuel, Sarah, Roman und Erol.
Außerdem bedanke ich mich bei meinen Freunden und Kollegen Eva, Christian, Julia, Daniel und Patrick.
Sehr großen Dank gilt Prof. Ropele, Prof. Fazekas, Prof. Enzinger und Prof. Schmidt für Ihr Vertrauen und Ihre Unterstützung.
Darüber hinaus möchte ich mich bei Christian, Lukas, Edith, und allen weiteren Kollegen der Neurologie bedanken.

Acronyms and Abbreviations

AD	Axial Diffusivity
ADC	Apparent Diffusion Coefficient
ALS	Amyotrophic Lateral Sclerosis
ALSFRS-R	Revised Amyotrophic Lateral Sclerosis Functional Rating Scale
ASPS	Austrian Stroke Prevention Study
ATR	Anterior Thalamic Radiation
CAB	Cingulum - Angular Bundle
CCG	Cingulum - Cingulate Gyrus Bundle
CHARMED	Composite Hindered and Restricted Model of Diffusion
CST	Corticospinal Tract
DKI	Diffusion Kurtosis Imaging
dMRI	Diffusion Magnetic Resonance Imaging
DSI	Diffusion Spectrum Imaging
DTI	Diffusion Tensor Imaging
DWI	Diffusion Weighted Imaging
FA	Fractional Anisotropy
FMAJOR	Corpus Callosum - Forceps Major
FMINOR	Corpus Callosum - Forceps Minor
FSL	FMRIB Software Library
GM	Gray Matter
ILF	Inferior Longitudinal Fasciculus
MD	Mean Diffusivity
MRI	Magnetic Resonance Imaging
NODDI	Neurite Dispersion and Density Imaging
PGSE	Pulsed Gradient Spin Echo
RD	Radial Diffusivity
RF	Radio Frequency
ROI	Region of Interest
SLFP	Superior Longitudinal Fasciculus - Parietal Bundle
SLFT	Superior Longitudinal Fasciculus - Temporal Bundle
SS-EPI	Single-Shot Echo Planar Imaging

TBSS	Tract-Based Spatial Statisctics
TRACULA	Tracts Constraints by Underlying Anatomy
UNC	Uncinate Fasciculus
WM	White Matter

List of Figures

Figure 1: Schematic representation of pulsed gradient spin echo sequence (PGSE), with diffusion time Δ, and paired rectangular gradients of strength G, and duration δ (adapted from [26])....... 5

Figure 2: Schematic representation of single-shot echo planar imaging (SS-EPI), where all k-space lines are collected with a single trajectory by bipolar readout gradients, here depicted in blue (adapted from [26]). 6

Figure 3: Illustration of readout segmented EPI. The here shown 5 shot EPI acquisition divides the k-space into 5 segments (adapted from [34]). 7

Figure 4: Three-dimensional geometric representation of the diffusion tensor as an ellipsoid described by its eigenvalues ($\lambda 1$, $\lambda 2$, and $\lambda 3$), and their corresponding eigenvectors ($\boldsymbol{\varepsilon}1$, $\boldsymbol{\varepsilon}2$, and $\boldsymbol{\varepsilon}3$) [23, 38]....... 12

Figure 5: Bayesian framework, consists of parameters from the local partial volume model (red dashed box, with Y represents the measured data, $S0$ is the non-diffusion-weighted signal, d is the diffusivity, f the contribution fraction, θ, ϕ are the fiber direction and orientation, and Σ and Λ represent the scale parameters), and the global parameters(blue dashed box, including the fiber connection $\mathcal{F}$, the existance of connection $\mathcal{C}$, the tract location $\mathcal{L}$, and the control points $\mathcal{K}$) (adapted from [17]). 24

Figure 6: Representation of global parameters for the connection of regions $\mathcal{R}1$ and $\mathcal{R}2$ at the locations $\mathcal{L}1$ and $\mathcal{L}2$, by the fiber pathway $\mathcal{F}12$, with $\mathcal{K}$ control points (adapted from [17]). 25

Figure 7: Three-dimensional representation of all 18 reconstructed WM tracts in relation to the anterior (A), posterior (P), superior (S), and inferior (I) directions. 28

Figure 8: Reconstruction of WM tracts dependent on number of diffusion encoding gradients based on SS-EPI dataset. Here shown from left to right are front, side, and top view. Orientation of 3D tracts in relation to anterior (A), posterior (P), superior (S), inferior (I), left (L), and right (R) directions. 29

Figure 9: Reconstruction of WM tracts dependent on number of diffusion encoding gradients based on readout segmented EPI dataset. Here shown from left to right are front, side, and top view. Orientation of 3D tracts in relation to anterior (A), posterior (P), superior (S), inferior (I), left (L), and right (R) directions. 30

Figure 10: Change of FA in all reconstructed fiber tracts from SS-EPI dataset over the number of applied diffusion gradients (# Directions). Here shown are mean values and standard deviation for all applied number of directions. Corresponding structures are shown in the same color, but with different mean value markers and different line shape for left (lh) and right (rh) hemisphere or anterior and posterior orientation. 31

Figure 11: Change of MD in all reconstructed fiber tracts from SS-EPI dataset over the number of applied diffusion gradients (# Directions). Here shown are mean values and standard deviation for all applied number of directions. Corresponding structures are shown in the same color, but with different mean value markers and different line shape for left (lh) and right (rh) hemisphere or anterior and posterior orientation. 32

Figure 12: Change of RD in all reconstructed fiber tracts from SS-EPI dataset over the number of applied diffusion gradients (# Directions). Here shown are mean values and standard deviation for all applied number of directions. Corresponding structures are

shown in the same color, but with different mean value markers and different line shape for left (lh) and right (rh) hemisphere or anterior and posterior orientation. 33
Figure 13: Change of AD in all reconstructed fiber tracts from SS-EPI dataset over the number of applied diffusion gradients (# Directions). Here shown are mean values and standard deviation for all applied number of directions. Corresponding structures are shown in the same color, but with different mean value markers and different line shape for left (lh) and right (rh) hemisphere or anterior and posterior orientation. 34
Figure 14: Change of FA in all reconstructed fiber tracts from readout segmented EPI dataset over the number of applied diffusion gradients (# Directions). Here shown are mean values and standard deviation for all applied number of directions. Corresponding structures are shown in the same color, but with different mean value markers and different line shape for left (lh) and right (rh) hemisphere or anterior and posterior orientation.......................... 35
Figure 15: Change of MD in all reconstructed fiber tracts from readout segmented EPI dataset over the number of applied diffusion gradients (# Directions). Here shown are mean values and standard deviation for all applied number of directions. Corresponding structures are shown in the same color, but with different mean value markers and different line shape for left (lh) and right (rh) hemisphere or anterior and posterior orientation.......................... 36
Figure 16: Change of RD in all reconstructed fiber tracts from readout segmented EPI dataset over the number of applied diffusion gradients (# Directions). Here shown are mean values and standard deviation for all applied number of directions. Corresponding structures are shown in the same color, but with different mean value markers and different line shape for left (lh) and right (rh) hemisphere or anterior and posterior orientation.......................... 37
Figure 17: Change of AD in all reconstructed fiber tracts from readout segmented EPI dataset over the number of applied diffusion gradients (# Directions). Here shown are mean values and standard deviation for all applied number of directions. Corresponding structures are shown in the same color, but with different mean value markers and different line shape for left (lh) and right (rh) hemisphere or anterior and posterior orientation.......................... 38
Figure 18: Change of FA in all reconstructed fiber tracts from normal healthy subjects over age. Here shown are mean values and standard deviation for every decade in age. Corresponding structures are shown in the same color, but with different mean value markers and different line shape for left (lh) and right (rh) hemisphere or anterior and posterior orientation.......................... 39
Figure 19: Change of MD in all reconstructed fiber tracts from normal healthy subjects over age. Here shown are mean values and standard deviation for every decade in age. Corresponding structures are shown in the same color, but with different mean value markers and different line shape for left (lh) and right (rh) hemisphere or anterior and posterior orientation.......................... 40
Figure 20: Change of RD in all reconstructed fiber tracts from normal healthy subjects over age. Here shown are mean values and standard deviation for every decade in age. Corresponding structures are shown in the same color, but with different mean value markers and different line shape for left (lh) and right (rh) hemisphere or anterior and posterior orientation.......................... 41

Figure 21: Change of AD in all reconstructed fiber tracts from normal healthy subjects over age. Here shown are mean values and standard deviation for every decade in age. Corresponding structures are shown in the same color, but with different mean value markers and different line shape for left (lh) and right (rh) hemisphere or anterior and posterior orientation.. 42

List of Tables

Table 1: Tract specific group analysis results of DTI properties in 18 WM tracts. Here provided are mean values ± standard deviation. Values for MD, RD, and AD are presented in $10 - 3\ mm2s - 1$. 44

1 Introduction

Diffusion magnetic resonance imaging (dMRI), or diffusion weighted imaging (DWI), is a quantitative magnetic resonance imaging (MRI) technique which provides unique image contrast. It probes the tissue microstructure by measuring the signal attenuation due to the random motion of water, even though images are acquired on a macroscopic scale. [1, 2]

DWI has many applications and was employed to investigate brain white matter (WM) and gray matter (GM), the spinal cord and nerves, as well as the heart and other muscles [2]. It has gained incredible popularity in clinical research and routine since it can depict microstructural tissue changes where other methods show lower sensitivity, or even fail to identify hallmarks [1, 3]. Since its development in the 1980s, dMRI has been used to study brain ischemia, brain development and aging, cancer, neurodegenerative diseases, such as multiple sclerosis, Alzheimer's disease and amyotrophic lateral sclerosis (ALS), and other disorders [3–5].

The standard DWI methods have been extended by Basser et al. [6] in 1994 by introducing of the diffusion tensor method, which lead to diffusion tensor imaging (DTI). Compared to standard DWI, DTI has the advantage to better describe the anisotropic diffusion properties of biologic tissue. The diffusion tensor can be diagonalized and represented as an ellipsoid, where its shape and orientation is described by its three eigenvalues and eigenvectors [7, 8]. Different diffusion parameters can be derived from these eigenvalues, which have different geometrical interpretation and provide information about diffusion anisotropy [9, 10]. However, these parameters are not able to map the complex configuration and structure of biological tissue. Therefore, more sophisticated, higher order models and representations are needed to overcome these limitations and give a more detailed and in-depth view of the biological microstructure [11–13].

Fiber tractography is a method which gives the ability to non-invasively investigate and visualize fiber pathways. It maps and tracks the direction of various fibrous tissue types, and is most commonly used to analyze WM pathways in the brain [14, 15]. This is done under the assumption that the fiber direction is parallel to the direction of highest diffusion within a voxel [1, 4, 14, 15]. First approaches used straight forward propagation techniques, where the largest eigenvalue of the local diffusion tensor and its corresponding eigenvector were used to reconstruct the trajectories of WM pathways which are called streamlines [4]. However, these deterministic algorithms do not account for the complex tissue microstructure and have trouble tracking fiber bundles in the presence of image noise and artifacts. Therefore, probabilistic tractography algorithms are needed, which incorporate higher order diffusion models [14, 15]. These local tractography approaches are fast, computational inexpensive, and are best suited to investigate the ensemble of all possible connections originating from a seed point. However, these approaches have the disadvantage that small errors can accumulate and progress along the fiber tracts [14, 16]. Global tractography algorithms were, therefore, implemented as an alternative, which promised better stability with respect to imaging artifacts. These global methods reconstruct all fiber trajectories simultaneously by optimizing a function to best fit the measured data [14]. Furthermore, by presuming that two regions of interest are connected, it is possible to reconstruct and identify specific WM pathways [17].

Nevertheless, all the aforementioned methods require a user with neuroanatomical expertise to manually interact with the data in order to reconstruct fiber pathways. This is very time consuming for larger tractography studies with multiple fiber tracts, and reduces stability and reliability [16, 18, 19]. To overcome this issue, Yendiki and colleagues developed TRACULA (TRActs Constrianed by UnderLying Anatomy) [16], which allows to automatically identify and reconstruct 18 major WM tracts based on a high resolution T_1-weighted scan, by utilizing global probabilistic tractography.

Therefore, this thesis is aimed on the implementation of TRACULA, as well as on the evaluation of this automated global probabilistic tractography tool regarding its stability, reliability, and possible application in clinical practice. To evaluate its stability, the software was applied on a dataset with varying spatial resolution and number of diffusion encoding gradient directions. Furthermore, TRACULA was performed on larger datasets of an ongoing community-dwelling study on aging [20, 21] and in a multimodal ALS study [22] to demonstrate its reliability and potential in clinical use.

2 Theory

2.1 Diffusion Principles

Diffusion is described as the random transport of particles through thermal motion, also known as Brownian motion. In general, diffusion is defined in terms of concentration gradients of molecules. This general description is expressed by Fick's laws of diffusion. However, thermally induced motion even takes place in absence of concentration gradients and is often referred to as self-diffusion in general physics. This type of diffusion occurs in biologic tissue where water moves within water, and is of interest in dMRI since its length scale is of the same order of magnitude as of biological microstructures [2, 23–26].

The random motion of water can be characterized by the relative displacement $\boldsymbol{R}$ of a water molecule, which moves from position $\boldsymbol{r}$ to $\boldsymbol{r}'$ [23, 27, 28]:

$$\boldsymbol{R} = (\boldsymbol{r}' - \boldsymbol{r}). \tag{1}$$

The ensemble average propagator or displacement probability density function that a particle undergoes this displacement $\boldsymbol{R}$ within a certain time t is given by:

$$\mathrm{P}(\boldsymbol{R}, t) = \int P(\boldsymbol{r}, \boldsymbol{r}', t)\rho(\boldsymbol{r})d\mathbf{r}, \tag{2}$$

where $\rho(\boldsymbol{r})$ is the initial molecule density and $P(\boldsymbol{r}, \boldsymbol{r}', t)$ is the conditional probability of finding a molecule at position $\boldsymbol{r}'$ with originates from $\boldsymbol{r}$ [23, 27, 28].

In case of free diffusion, the ensemble average propagator is Gaussian distributed and expressed as [23, 29, 30]:

$$P(\boldsymbol{R}, t) = \frac{1}{\sqrt{(4D\pi t)^3}} \exp\left(-\frac{|\boldsymbol{R}|^2}{4Dt}\right), \tag{3}$$

with D known as the diffusion coefficient.

The mean squared dynamic displacement $\langle R^2 \rangle$ is then given by [25, 29, 30]:

$$\langle R^2 \rangle = \int_{-\infty}^{+\infty} R^2 P(\boldsymbol{R}, t) d\boldsymbol{R} = 6Dt, \tag{4}$$

which is proportional with time. From Equation (4) the diffusion coefficient can then be calculated as follows:

$$D = \frac{\langle R^2 \rangle}{6t}. \tag{5}$$

For a simple liquid, such as water, the diffusion coefficient is $3 \cdot 10^{-3}\ mm^2 s^{-1}$ at $37°C$ [26]. However, for biological tissues with anisotropic diffusion, the mean squared dynamic displacement does not scale linearly with time, and therefore a more complex representation of the diffusion coefficient is needed which will be considered later in this chapter [23, 30].

2.2 dMRI Measurement

To measure the diffusion coefficient, Stejskal and Tanner introduced diffusion weighting by adding two identical gradient pulses on both sides of the refocusing pulse of a spin echo sequence [23, 31]. This method is called the pulsed gradient spin echo (PGSE) sequence and a simple schematic representation is depicted in Figure 1, where, for simplicity, the paired gradients are assumed to have rectangular shape with strength G and duration δ [2, 30]. In principle, the PGSE sequence measures the signal attenuation which arises from self-diffusion during a diffusion time Δ [23, 26, 30].

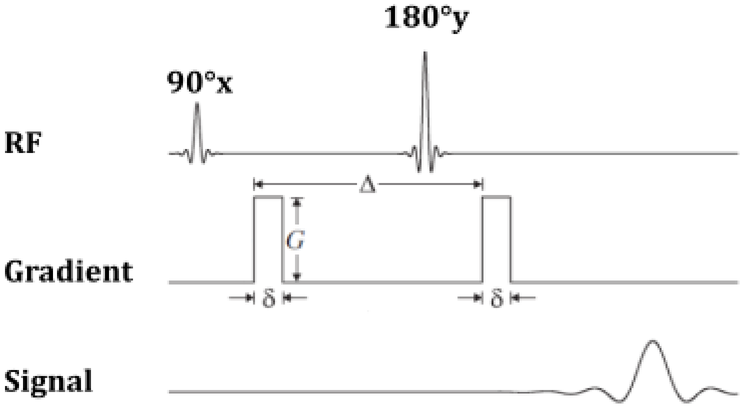

Figure 1: Schematic representation of pulsed gradient spin echo sequence (PGSE), with diffusion time Δ, and paired rectangular gradients of strength G, and duration δ (adapted from [26]).

The concept of the PGSE sequence can be understood in the following way. All spins within an ensemble are excited and flipped in the transversal plane by the first radio frequency (RF) pulse. During the application of the first gradient pulse, the spins are modulated and acquire a phase shift depending on their position. A refocusing RF pulse is applied afterwards, which inverts the phase of the spins and reverses the direction of precession. The second diffusion gradient is employed after a diffusion time from the beginning of the first one, which demodulates the spins and induces another phase shift. For static spins, the two applied gradient pulses cancel each other out and a maximum echo signal is recorded. However, if some spins have diffused, the two phase shifts are different depending on the degree of displacement, which leads to incomplete refocusing and an amplitude attenuation of the echo signal [25, 30].

It should be noted that generally the diffusion gradients can be applied in any direction of the Cartesian coordinate system, while, for simplicity, the gradients presented here were applied in one main coordinate direction.

Single-shot echo planar imaging (SS-EPI) is the most common method for image acquisition in dMRI. It is a fast readout procedure were all k-space lines are sampled with a single alternating trajectory reversal by using bipolar gradients (Figure 2) [2, 26, 32].

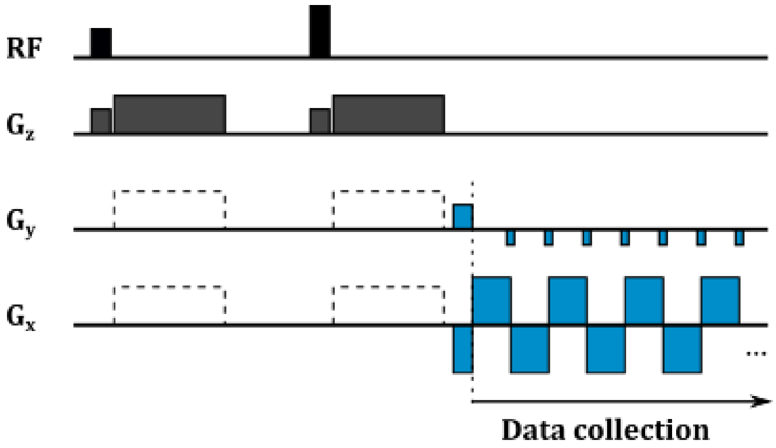

Figure 2: Schematic representation of single-shot echo planar imaging (SS-EPI), where all k-space lines are collected with a single trajectory by bipolar readout gradients, here depicted in blue (adapted from [26]).

However, SS-EPI has the limitation of exhibiting low spatial resolution. Therefore, readout segmented EPI has been introduced as an alternative for dMRI to acquire high resolution images. In readout segmented EPI, the k-space is split in segments which are then acquired in readout direction (Figure 3). This gives the advantage of decreasing distortion and blurring artefacts, and further enables higher possible spatial resolution with the downside of resulting in a longer scan time [33, 34].

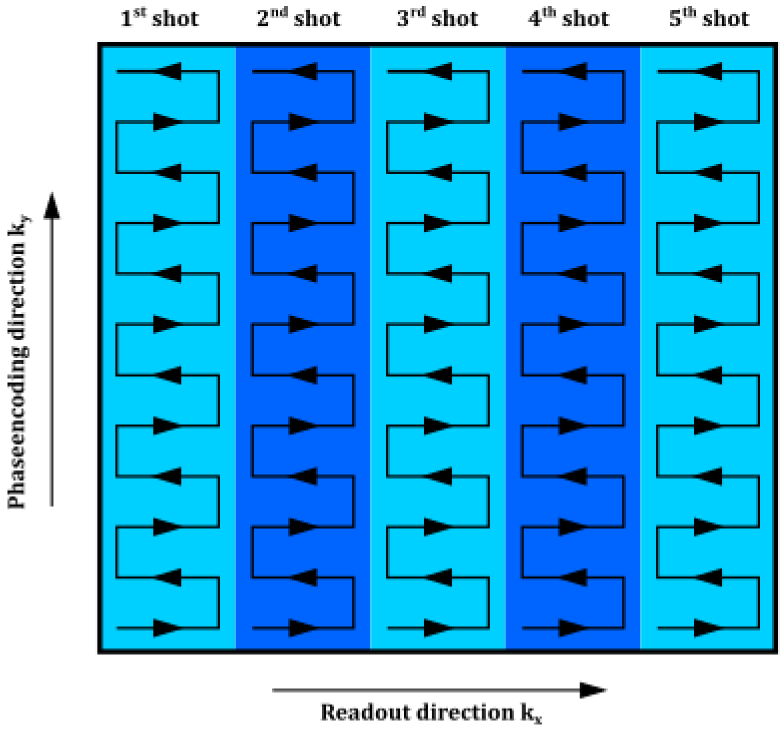

Figure 3: Illustration of readout segmented EPI. The here shown 5 shot EPI acquisition divides the k-space into 5 segments (adapted from [34]).

2.3 DWI

By applying diffusion weighing as described in Section 2.2, a signal S_b of the following expression is measured [10, 35]:

$$S_b = S_0 e^{-bD}, \tag{6}$$

with S_0 being the signal without diffusion weighting, D being the diffusion coefficient, whereby the b-value or b-factor is defined as:

$$b = (\gamma G \delta)^2 \left(\Delta - \frac{\delta}{3}\right), \tag{7}$$

for rectangular diffusion gradients, as shown in Figure 1, where γ is the gyromagnetic ratio, G is the gradient amplitude, δ is the gradient pulse width, and Δ is the time between the two gradients.

The diffusion coefficient D can then be calculated by:

$$D = \frac{\ln\left(\frac{S_0}{S_b}\right)}{b}. \tag{8}$$

Nevertheless, for complex tissue structures, the displacement is no longer proportional to the diffusion time, which results in a lower diffusion coefficient compared to isotropic liquids. Thus, by applying this method, the calculated diffusion coefficient should be referred to as the apparent diffusion coefficient (ADC) [23, 26, 36].

In clinical practice, multiple diffusion-weighted images from different b-factors are collected. By acquiring at least 4 diffusion-weighted images (one without diffusion-weighting, and three with a b-factor probing in three orthogonal directions), several different, rotationally invariant measures can be derived which are used for clinical diagnosis [15, 37].

The simplest one being the isotropic or combined DWI, which is the geometric average of the three orthogonal measured diffusion-weighted images [15, 37]

$$S_{DWI} = \sqrt[3]{S_x S_y S_z}, \tag{9}$$

with S_x, S_y ,and S_z representing the measured signals along the three different directions. From this merit, the mean ADC (also written as $\langle ADC \rangle$), often referred to as the ADC in a clinical setting, can be extracted

$$\langle ADC \rangle = \ln \frac{\left(\frac{S_0}{S_{DWI}}\right)}{b}, \tag{10}$$

which can also be calculated from

$$\langle ADC \rangle = \frac{\mathrm{ADC}_x + ADC_y + ADC_z}{3}, \tag{11}$$

where the sum of the ADCs is also known as trace ADC [8, 15, 25, 37].

2.4 DTI

A more proper method for the characterization of diffusion in anisotropic media which also accounts for the orientation dependency was introduced by Basser and colleagues who used the diffusion tensor $\boldsymbol{D}$ [6, 23, 38]. The diffusion tensor $\boldsymbol{D}$ is a 3 × 3 vector matrix of the form:

$$\mathbf{D} = \begin{pmatrix} D_{xx} & D_{xy} & D_{xz} \\ D_{yx} & D_{yy} & D_{yz} \\ D_{zx} & D_{zy} & D_{zz} \end{pmatrix}, \tag{12}$$

where diagonal elements represent the magnitude of diffusivity along x-, y-, and z-direction, while the off-diagonal terms illustrate the magnitude of diffusion in one direction emerging from a concentration gradient in orthogonal direction [6, 15, 23, 38]. Since the diffusion tensor is symmetric (i.e. $D_{ij} = D_{ji}$), it has 6 independent elements, and can be determined from at least 7 DWI measurements, one without ($b = 0\ mm^2s^{-1}$) and 6 with diffusion encoding ($b > 0\ mm^2s^{-1}$) in 6 non-collinear directions [6, 38].

Basser and colleagues showed the determination of the diffusion tensor $\boldsymbol{D}$ by solving the following voxel wise linear system [6, 39]:

$$\mathbf{x} = \boldsymbol{B}\alpha. \tag{13}$$

Where the observed data S from N measurements are represented as an $N \times 1$ column vector, $\boldsymbol{x}$:

$$\boldsymbol{x} = \begin{pmatrix} \ln(S_1) \\ \ln(S_2) \\ \vdots \\ \ln(S_N) \end{pmatrix}. \tag{14}$$

The $N \times 7$ matrix $\boldsymbol{B}$ is described by the elements of the b-matrix, which is a 3D representation of the b-factor:

$$\boldsymbol{B} = \begin{pmatrix} -b_{xx1} & -b_{yy1} & -b_{zz1} & -2b_{xy1} & -2b_{xz1} & -2b_{yz1} & 1 \\ \vdots & \vdots & \vdots & \vdots & \vdots & \vdots & \vdots \\ -b_{xxN} & -b_{yyN} & -b_{zzN} & -2b_{xy1} & -2b_{xzN} & -2b_{yzN} & 1 \end{pmatrix}. \tag{15}$$

And the column vector α is defined by the 6 independent diffusion tensor elements and the logarithmic signal of the non-diffusion weighted measurement S_0

$$\alpha = [D_{xx} \quad D_{yy} \quad D_{zz} \quad D_{xy} \quad D_{xz} \quad D_{yz} \quad \ln(S_0)]^T. \tag{16}$$

A different approach to determine the diffusion tensor is by defining the column vector, $\boldsymbol{d}$ [39, 40]:

$$\mathbf{d} = [D_{xx} \quad D_{yy} \quad D_{zz} \quad D_{xy} \quad D_{xz} \quad D_{yz}]^T. \tag{17}$$

Information about the normalized diffusion gradient directions g_{xi}, g_{yi}, and g_{zi} is stored in the $M \times 6$ matrix, $\boldsymbol{H}$, for a total number of M diffusion weighted measurements.

$$\boldsymbol{H} = \begin{pmatrix} g_{x1}^2 & g_{y1}^2 & g_{z1}^2 & 2g_{x1}g_{y1} & 2g_{x1}g_{z1} & 2g_{y1}g_{z1} \\ g_{x2}^2 & g_{y2}^2 & g_{z2}^2 & 2g_{x2}g_{y2} & 2g_{x2}g_{z2} & 2g_{y1}g_{z2} \\ \vdots & \vdots & \vdots & \vdots & \vdots & \vdots \\ g_{xM}^2 & g_{yM}^2 & g_{zM}^2 & 2g_{xM}g_{yM} & 2g_{xM}g_{zM} & 2g_{yM}g_{zM} \end{pmatrix} \tag{18}$$

The examined data $\boldsymbol{Y}$ are represented as their measured ADCs (see Equation (8)):

$$\boldsymbol{Y} = \left[\frac{\ln\left(\frac{S_0}{S_1}\right)}{b} \quad \frac{\ln\left(\frac{S_0}{S_2}\right)}{b} \quad \cdots \quad \frac{\ln\left(\frac{S_0}{S_M}\right)}{b} \right]^T, \tag{19}$$

and, the voxel wise linear system is then given by

$$\boldsymbol{Y} = \boldsymbol{Hd}. \tag{20}$$

For the case of applying exactly 6 diffusion weighted directions there exists an exact solution to Equation (20). This basic inverse problem can be solved accordingly by calculating the inverse of the $\boldsymbol{H}$ matrix [39, 40]:

$$(\boldsymbol{H}^{-1}\boldsymbol{H})\boldsymbol{d} = \boldsymbol{d} = \boldsymbol{H}^{-1}\boldsymbol{Y}. \tag{21}$$

Usually more than 6 encoding directions are applied to increase the stability for the determination of the diffusion tensor. This results in an overdetermined inverse problem where the matrix $\boldsymbol{H}$ is not squared anymore and the true inverse $\boldsymbol{H}^{-1}$ does not exist. By using an unweighted linear least-squares fit this overdetermined system can be solved accordingly [39, 40]:

$$\boldsymbol{d} = (\boldsymbol{H}^T\boldsymbol{H})^{-1}\boldsymbol{H}^T\boldsymbol{Y}. \tag{22}$$

Furthermore, by using the covariance matrix it is also possible to perform a weighted linear least-squares fit which should give even more correct results [6, 39].

The computed diffusion tensor can be decomposed in its eigenvalues (λ_1, λ_2, and λ_3, in descending order of magnitude), as well as their corresponding eigenvectors ($\boldsymbol{\varepsilon}_1$, $\boldsymbol{\varepsilon}_2$, and $\boldsymbol{\varepsilon}_3$), and can be further geometrically represented as an ellipsoid (Figure 4) [23, 38].

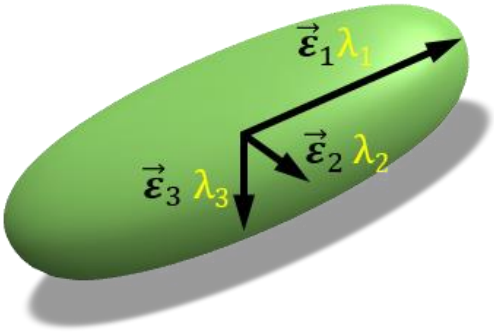

Figure 4: Three-dimensional geometric representation of the diffusion tensor as an ellipsoid described by its eigenvalues (λ_1, λ_2, and λ_3), and their corresponding eigenvectors ($\boldsymbol{\varepsilon}_1$, $\boldsymbol{\varepsilon}_2$, and $\boldsymbol{\varepsilon}_3$) [23, 38].

From these eigenvalues several different diffusion metrics like, mean diffusivity (MD), axial and radial diffusivity (AD and RD), and fractional anisotropy (FA) can be derived within a voxel to better characterize the diffusion properties [9, 10, 15, 23]. The mean diffusivity is the simplest measure and represents the average value of diffusion within a voxel,

$$MD = \frac{\lambda_1 + \lambda_2 + \lambda_3}{3}. \tag{23}$$

Diffusion rates along the main, and transversal directions are the axial and radial diffusivities which are described by the largest eigenvalue, and the average of the two smaller eigenvalues,

$$AD = \lambda_1, \tag{24}$$

$$RD = \frac{\lambda_2 + \lambda_3}{2}. \tag{25}$$

The fractional anisotropy illustrates the degree of directional diffusion,

$$FA = \frac{\sqrt{(\lambda_1 - \lambda_2)^2 + (\lambda_2 - \lambda_3)^2 + (\lambda_3 - \lambda_1)^2}}{\sqrt{2(\lambda_1^2 + \lambda_2^2 + \lambda_3^2)}}, \tag{26}$$

where $\mathrm{FA} = 0$ would mean isotropic diffusion, and $\mathrm{FA} = 1$ complete anisotropic, directional diffusion [9, 10, 15, 23]. Often maps of FA values are superimposed by their main eigenvector to indicate the principle diffusion direction. In detail, by assigning each coordinate axis (x, y, and z) to the colors red, green, and blue, it is possible to generate FA maps where the fiber orientation controls the hue, and the extent of anisotropy conducts the brightness of each pixel [10, 15, 23].

2.5 Higher Order Diffusion Models

The diffusion tensor is a very useful and elegant model to probe the microstructural configuration of tissue such as myelination and density. However, since it does not account for multiple diffusion compartments and restricted diffusion, as well as multiple fibers within a voxel, it has been shown to be insufficient to assess more complex tissue microstructure and fiber configuration. Therefore, more sophisticated, so called higher order models have been established to overcome these limitation [2, 11, 13, 23, 26, 41].

These higher order models have been mainly separated into two types of concepts. The first type works on the basis of finding a model which best describes the underlying biophysical properties and microstructural features of a specific tissue type [11, 41]. These model driven approaches consider the signal as a sum from several contributions, and relate it directly to microstructural heterogeneity and microscopic features by utilizing compartmentation and modeling as basic geometric objects. They rely on assumptions, approximations and constraints to simplify the general picture of natural complexity. Such models are for instance the ball-and-stick model, the composite hindered and restricted models of diffusion (CHARMED), AxCaliber, and the neurite dispersion and density imaging (NODDI) tissue model, just to name a few. These types of models are in general more important than signal based approaches, which are the second type of approaches [11, 41]. Signal models are model-independent mathematical representations of the measurement which are represented as functions with a set of adjustable parameters and coefficients. They rely on very few assumptions and do not describe any underlying physical impression. These models include for example diffusion kurtosis imaging (DKI), q-space imaging, and diffusion spectrum imaging (DSI) [11, 41].

To incorporate any of the aforementioned concepts a higher amount of information is needed. This is realized by increasing the number of diffusion encoding directions, as well as the number of sampled b-values, and sampling the DWI signal on a Cartesian grid or on several spheres of the diffusion space. Though, this increases the acquisition time and restricts its possible clinical application [13, 42].

2.6 Fiber Tractography

Fiber tractography, or often only referred to as tractography, is a technique which enables the possibility to non-invasively visualize and investigate in vivo fiber trajectories of fibrous tissue such as brain WM in 3D. The general assumption in tractography is that every voxel is characterized by a single primary fiber direction which is parallel to the major diffusion direction [1, 14, 15].

In principal, tractography is performed in three main steps which are the seeding, the tracking, and the termination of fiber trajectories [2, 13, 14].

A seed point is the defined starting location where the fibers are being tracked. Generally, a preferred region of interest (ROI) is specified which defines several seed points. These ROIs are usually manually defined by a user. This however, is very time consuming for multiple tracts and requires a user with vast neuroanatomical expertise, as well as reduces stability and reliability [14, 16, 18, 19]. To overcome this issues, ROIs can also be derived from anatomic atlases, which define certain brain structures or cortical regions. Alternatively, cortical activation maps determined from functional MRI can be used as ROIs. This approach might seem very elegant since it allows to analyze and correlate structural and functional connectivity. Nevertheless, it may be difficult to implement this approach since the primary diffusion direction of GM is less prominent than in WM [13, 14].

There exist several approaches to terminate a fiber streamline. The most common method is by defining a lower threshold for diffusion anisotropy, usually FA. For example, if the FA values of a voxel is below this pre-defined threshold the trajectory streamline will be stopped. Since it is well-known that fiber tracts in the brain do not take sharp turn, it is possible to impose an angular threshold. In this case, the propagation of a trajectory is terminated when the angle between the initial and subsequent direction is above this threshold. Finally, it is possible to apply anatomical constrains to prevent streamlines from entering unreasonable areas [13, 14].

The tract propagation can be realized with different types of methods and tractography algorithms. The earliest and simplest methods were deterministic algorithms, which use the orientation information of the diffusion tensor. These approaches reconstruct fiber trajectories represented as space curves step-by-step by integrating the partial differential equation:

$$\frac{\partial \boldsymbol{r}(s)}{\partial s} = \boldsymbol{\varepsilon}_1\big(\boldsymbol{r}(s)\big), \tag{27}$$

where $\boldsymbol{r}(s)$ is the streamline at point s, and $\boldsymbol{\varepsilon}_1$ is the corresponding principal eigenvector of the diffusion tensor [2, 14, 43]. The simplest way of solving this problem is by using Taylor series expansion, which lead to the form [2, 43]:

$$\boldsymbol{r}(s_1) \approx \boldsymbol{r}(s_0) + \alpha\boldsymbol{\varepsilon}_1\big(\boldsymbol{r}(s_0)\big). \tag{28}$$

A different approach to solve this partial differential equation is by using 2nd or 4th order Runge-Kutta methods, which result in smoother trajectories compared to Taylor series expansion [2, 43]. Nevertheless, these deterministic approaches do not consider multiple fibers within a voxel, as well as complex tissue microstructure. Furthermore, image noise and artifacts cause uncertainty in the orientation of the diffusion tensor, which lead to streamline errors [13–15]. To resolve these issues, probabilistic fiber tractography algorithms are used. These algorithms work on the basis of higher order diffusion models, and use a local orientation distribution function for reconstructing fiber trajectories [13–15]. All the aforementioned local tractography algorithms are computational fast, simple to implement, widely used, and best suited for exploratory studies. However, they have the disadvantage of small errors accumulating and progressing along the fiber streamlines, and further changing to overall appearance of the tract [14, 16]. Global tractography approaches provide an alternative solution, which promise superior reconstruction and tracking stability. These types of algorithms reconstruct the fiber trajectories by using the information on diffusion direction of all voxels simultaneously, and optimize a function that best fits the acquired data. In addition, it is possible to reconstruct and identify particular WM pathways by constraining the connection of two ROIs [14, 16, 17].

2.7 Stroke

Stroke is a heterogeneous disorder originating from various pathologies, and affects the blood circulation in the brain. It can be subdivided into two distinct types, the first being ischemic stroke, which results from occluded blood flow, and is responsible for more than 80% of the overall stroke incidence. Hemorrhagic stroke is the other lesser portion of stroke occurrence, and is the corollary of blood intruding the brain or subarachnoid space [44].

Both types of stroke, and their numerous subtypes feature distinct underlying pathologies which are the direct consequence of different risk factors. The identification and monitoring of these risk factors is the key to prevention and treatment of stroke. Therefore, the Austrian Stroke Prevention Study (ASPS) aims on the investigation and assessment of already established and future cerebrovascular risk factors. It is an ongoing monocentric prospective long-term community-dwelling study in a central European population, which incorporates a comprehensive diagnostic examination, including MRI [20, 21].

Diffusion MRI is the most successful application in acute brain ischemia, and the imaging technique of choice to manage patients suffering from stroke [4]. It was shown that water diffusion decreased significantly in the very early phase of acute brain ischemia. Furthermore, in comparison to other imaging methods such as T_2-weighted images and X-ray computed tomography, dMRI can detect microstructural changes much quicker, or even reveal alterations were others fail [1, 4]. Therefore, dMRI has been proven to be an effective tool for the detection, classification, monitoring, and treatment of both, acute and chronic, patients [1, 4].

2.8 ALS

ALS is a fast progressing, invariable, relentlessly lethal neurodegenerative disease, which results in the degeneration of the upper and lower motor neuron system. The prevalence of ALS is two to three people within 100,000 of the general European population and the majority of patients die within three years after diagnosis. It is possible to further classify ALS according to the site of onset, into limb and bulbar onset ALS. The clinical representation of ALS is dependent on the disease onset, and includes for example spasticity, dysphagia, and respiratory problems [45, 46].

Currently, the diagnosis of ALS is based on distinctive clinical and electrophysiological features, according to the revised El Escorial criteria [47]. MRI, and in particular DTI has been shown to be one of the most promising and sensitive imaging techniques to probe ALS related microstructural tissue changes. Accordingly, damage of the corticospinal tract (CST) has been identified as a pathologic hallmark feature of ALS. Moreover, microstructural tissue changes were observed in additional tracts which suggests that ALS pathologies advances in more widespread areas of the central nervous system [22, 48, 49]. Compared to other conventional MRI and imaging modalities, DTI showed a higher sensitivity and specificity in detecting ALS related pathologies also in other large widespread areas of WM, beyond the CST [22, 49, 50].

3 Methods

3.1 Subjects

To analyze the implication of varying spatial resolution and number of diffusion encoding gradients directions, MRI datasets of a single 32 years old male healthy volunteer were collected.

Furthermore, 212 healthy participants were selected from the ASPS cohort. Among which where 126 women and 85 men, within 38 and 81 years of age and a mean age of 64.7 ± 11.4 years. The complete ASPS cohort received a comprehensive clinical routine including clinical history, laboratory evaluation, cognitive testing, assessment of vascular risk factors, and MRI. None of the participants had any signs and history of neuropsychiatric disease, abnormal neurologic findings examined by a board-certified neurologist, heart failure, or uncorrected visual impairment. The study protocol was approved by the ethics committee of the Medical University of Graz, and signed consent were given by all participants.

ALS patients were recruited over a 6-year period to take part in an ongoing prospective study with an extensive clinical work-up, including MRI, and neurophysiologic examination by an expert. In total, the data from 27 patients were collected. All patients had definite ALS determination but were initially classified as possible and probable ALS according to the El Escorial criteria [47]. Their degree of functional impairment was characterized using the revised amyotrophic lateral sclerosis functional rating scale (ALSFRS-R), which uses 13 different elements with a score ranging from 48 (best) to 0 points (worst) [51]. Which resulted in an overall mean ALSFRS-R of 38.8 ± 8.7, within a mean disease duration of 16.1 ± 12.7 months. None of the participants showed any clinical indication for dementia. The study was approved by the ethics committee of the Medical University of Graz, and written informed consent were obtain from all subjects.

3.2 Data acquisition

All MRI measurements were performed on a Siemens Healthcare, Tim Trio 3 Tesla system (Siemens Healthcare, Erlangen, Germany), which is located at Department of Radiology of the Medical University of Graz, Austria.

3.2.1 Multiresolution dataset

Multiresolution datasets were acquired with a 32-channel head coil.

DWI was performed using a 2D diffusion weighted spin-echo sequence with a SS-EPI readout (TR/TE = 6200 ms/86 ms and NEX = 2), a GRAPPA acceleration factor of 2, and an image resolution of $2 \times 2 \times 3\ mm^3$. For diffusion modeling 64 independent diffusion sensitizing directions and two b-values (b = 0 and 1000 s/mm^2) were executed.

Additionally, a 2D readout segmented EPI spin-echo-based diffusion sequence (TR/TE = 11700 ms/76 ms and NEX = 1) was used to acquire higher resolution DWI data with 1.5 mm isotropic resolution. The diffusion was probed in 20 collinear direction, and two b-values (b = 0 and 1000 s/mm^2).

Structural images were obtained by using a T_1-weighted 3D MPRAGE sequence with 1 mm isotropic resolution (TR/TE/TI/flip angle = 1.9 s/2.15 ms/9° and FoV = 256 mm), and whole brain coverage.

3.2.2 Normal Healthy Subjects

All MRI measurements for ASPS participants were taken by using a 12-channel head coil array.

Diffusion data were collected using a 2D diffusion-weighted spin-echo sequence with single shot EPI readout (TR/TE = 6700 ms/95 ms and NEX = 4), GRAPPA acceleration factor of 2, and an image resolution of $2 \times 2 \times 3\ mm^3$. Twelve independent diffusion sensitizing direction and two b-values (b = 0 and 1000 s/mm^2) were applied to perform DTI and tractography.

A T_1-weighted 3D MPRAGE sequence with 1 mm isotropic resolution (TR/TE/TI/flip angle = 1.9 s/2.15 ms/9° and FoV = 256 mm) was applied to gain structural images.

The imaging protocol for volunteers of the ASPS included further imaging sequences which are beyond the scope of this thesis and not further discussed.

3.2.3 ALS

ALS patients underwent MRI by utilizing the identical imaging sequences as described in Section 3.2.2, and for convenience are not further mentioned here. Furthermore, the initial imaging procedure comprised of a more comprehensive MRI protocol for the evaluation of clinical status, and is not further indicated in this thesis.

3.3 Software implementation

TRACULA is a part of the FreeSurfer 5.3 software package [52], and uses several different software-wide integrated functions. Additionally, it utilizes some operation methods from the FMRIB Software Library (FSL), version 5.0.6 [53]. Therefore, all necessary software packages and software links which did not already exist, were implemented and established on an IBM x3500 M3 server system. The system was running an Intel Xeon X5690 processor with 6 cores and 12 threads at 3.47 GHz, 24 GB of RAM, and working a 64-bit Ubuntu 12.04 operating system.

3.4 Image analysis

3.4.1 Preprocessing

All acquired images were visually inspected ahead of processing, to prevent results being influenced by motion and other imaging artifacts. Afterwards, all scans were converted from DICOM to NIfTI format using dcm2nii [54]. This allowed for simpler and more convenient data handling.

Furthermore, dcm2nii extracts the normalized gradient directions and b-values into **.bvec** and **.bval** files, which are needed for the continuing processing. The extracted values in the **.bvec** and **.bval** files are presented in rows. Since TRACULA expects these values to be ordered in columns, they had to be transposed to be depicted in columns.

The reconstruction tool *recon-all*, which is included in the FreeSurfer software suite [52], was used, to perform automated reconstruction and labeling of distinctive brain regions. All technical details for these automated procedures have been described and evaluated previously [55–57]. Concisely, the reconstruction consisted of three main tasks based on the high resolution T_1-weighted scan. First, it generated WM and pial surfaces by voxel-wise classification. Therefore, every voxel got assigned to a WM or other than WM label based on its intensity and neighbor constraints. Furthermore, cutting planes were chosen to separate hemispheres and to remove the cerebellum, the brain stem and non-brain tissue. Afterwards, subcortical regions were segmented into around 40 unique structures. Finally, automatic parcellation was performed to identify every point of the entire cerebral cortex, and assigning it to one of the 85 separate units. Both, the subcortical segmentation and cortical parcellation use the same underlying procedure and basic algorithm. Each labeling procedure uses an individual atlas which is generated from manually labeled training sets of subjects which are mapped to a common space. Prior to labeling each individual input image is aligned to best match the anatomical atlases using affine and higher dimensional non-linear registration. Finally, each voxel gets assigned to a class label by using a Bayesian approach and prior information on the given atlases and alignment functions.

A python script was used to extract diffusion datasets with 6, 12, and 20 diffusion encoding direction for lower, and 6, and 12 sensitizing directions for higher resolution diffusion images of the multiresolution dataset. This script scans through the diffusion gradient vector file to find and extract the closest normalized gradient direction according to a template. The 6 template gradient directions were defined as described by Kingsley [58]. For the 12 direction template a sample gradient encoding scheme from the ASPS cohort was taken as a reference. The normalized diffusion directions from the high resolution diffusion scan were takes as a guide to extract a 20 direction dataset from the low resolution scan. The corresponding images were then extracted und combined into new 4D image stacks using *fslroi* and *fslmerge* from FSL [53]. After extraction, all 5 new created image stacks were scrutinized visually.

3.4.2 DTI and Fiber Tractography

To increase the statistical validity regarding the software stability, TRACULA was executed three times in every instance of the overall 7 single subject multiresolution datasets. Furthermore, it was performed on every normal healthy participant and ALS patient.

TRACULA was used for automatic diffusion parameter analysis and global probabilistic tractography. The whole procedure and all working steps have been presented and described previously [16]. Generally, the entire workflow consists of three main processing tasks which require the DWI data: preprocessing, model fitting, and pathway reconstruction.

The first action of preprocessing was eddy current and simple head motion correction. This was achieved by using FSL's *eddy_correct*, which registered every diffusion weighted volume of the series to the image without diffusion sensitization. After removing non-brain tissue with FSL's *bet*, all $b = 0$ images were registered to their corresponding T_1-weighted image by affine registration using FSL's *flirt*. Furthermore, by performing affine inter-subject registration of all individual T_1 scans to a common space, a diffusion-to-template transformation was achieved. Afterwards, masks for WM units and cortex labels were created based on the subcortical segmentation and cortical parcellation, and further transformed from the individual T_1 to the individual diffusion space by incorporating the afore computed transformation. The next preprocessing step was the computation of all DTI parameters (FA, MD, AD, and RD) by performing a least-squares fit using FSL's *dtifit*. Afterwards, the calculated scalar maps are transformed from the diffusion space into the template space with the earlier computed registration matrix. TRACULA relies on manually labeled training data to compute a priori pathway probabilities, which is the final preprocessing step. Additionally, the training subjects are used to obtain an initial guess of the location of the control points and the two trajectory ending ROIs for each pathway. These estimated initial control points were then mapped from template space into the individual diffusion spaces.

Model fitting was performed using FSL's *bedpostx* which fits the ball-and-stick model of diffusion [12] to the DWI data. This model has been introduced and described earlier [12, 59]. In general, the ball-and-stick model tries to model the underlying fiber structure which represents the form of diffusion and thus the measured signal. The most straightforward form of this model is a simple two-compartment partial volume model. Hence, the first compartment models isotropic diffusion of free water, whereas the second one models anisotropic diffusion along the fiber direction. The i^{th} measured diffusion-weighted signal μ_i, along a gradient direction $\boldsymbol{r}_i$, with b-value b_i, can therefore be written as [12]:

$$\mu_i = S_0 \left((1 - f) \exp(-b_i d) + f \ \exp(-b_i d \boldsymbol{r}_i^T \boldsymbol{RAR}^T \boldsymbol{r}_i) \right), \tag{29}$$

where S_0 is the signal without diffusion weighting, d is the diffusivity, f is the fraction signal contributed by anisotropic diffusion, and $\boldsymbol{RAR}^T$ is the anisotropic diffusion tensor along the fiber direction with orientation (θ, ϕ). For each voxel the noise is modeled separately as an independently identically distributed Gaussian, with zero mean and a standard deviation across measurements of σ. Thus, this model has a parameter set ω of six free parameters $(S_0, f, d, \theta, \phi, \sigma)$. However, in the above introduced partial volume model, only a single fiber orientation is considered for each voxel. Therefore, this model was expanded to deduce for multiple fiber configurations. Accordingly, the predicted measured DWI signal μ_i can be stated as [59]:

$$\mu_i = S_0\left(\left(1 - \sum_{j=1}^{N} f_j\right)\exp(-b_i d) + \sum_{j=1}^{N} f_j \exp\left(-b_i d \boldsymbol{r}_i^T \boldsymbol{R}_j \boldsymbol{A} \boldsymbol{R}_j^T \boldsymbol{r}_i\right)\right). \tag{30}$$

Again, S_0 is the non-diffusion-weighted signal, d is the diffusivity, b_i and $\boldsymbol{r}_i$ are the b-value and the gradient direction of the *i^th^* measurement, and f_j and $\boldsymbol{R}_j \boldsymbol{A} \boldsymbol{R}_j^T$ are the contribution fraction, and anisotropic diffusion tensor of the *j^th^* fiber orientation, and a maximum of *N* fibers. To fit the parameterized model to the data, the parameters can be considered as a probability density function. By using a Bayesian framework this function is called the posterior distribution on the parameters given the data:

$$\mathrm{P}(\omega|Y, M) = \frac{P(Y|\omega, M)\, P(\omega|M)}{P(Y|M)}, \tag{31}$$

where Y represents the data and M the model. However, calculating this probability density function, which include solving large integral is troublesome and not tractable analytically. Furthermore, using rejection sampling and importance sampling schemes, which draw samples in parameter space to solve the integrals numerically and overcome this problem, is computationally extensive and very slow. Therefore, the Markov Chain Monte Carlo sampling technique is used which addresses this time issue by suggesting samples preferably in areas of high probability. Additionally, by applying a Bayesian trick, known as automatic relevance determination, or shrinkage priors, it is possible to infer multiple fiber population only in cases where there is evidence in the data that they exist. Moreover, the use of automatic relevance determination is essential for this multi-compartment model, since it hinders the model from overfitting the data. In the here presented case of running *bedbostx* inside TRACULA, one isotropic and two anisotropic compartments were assumed to model the voxel-vise diffusion signal.

Automated WM pathway reconstruction was performed using a Bayesian model for global tractography. The pathway reconstruction relies on prior information which was extracted from a set of training subjects. This procedure has been reported and illustrated in an earlier paper by Yendiki et al. [16] and is based on a Bayesian framework developed by Jbabdi et al. [17]. Essentially, this model is composed from the local partial volume model, as described in the aforementioned paragraph, and global parameters. A graphical depiction of this Bayesian framework is depicted in Figure 5.

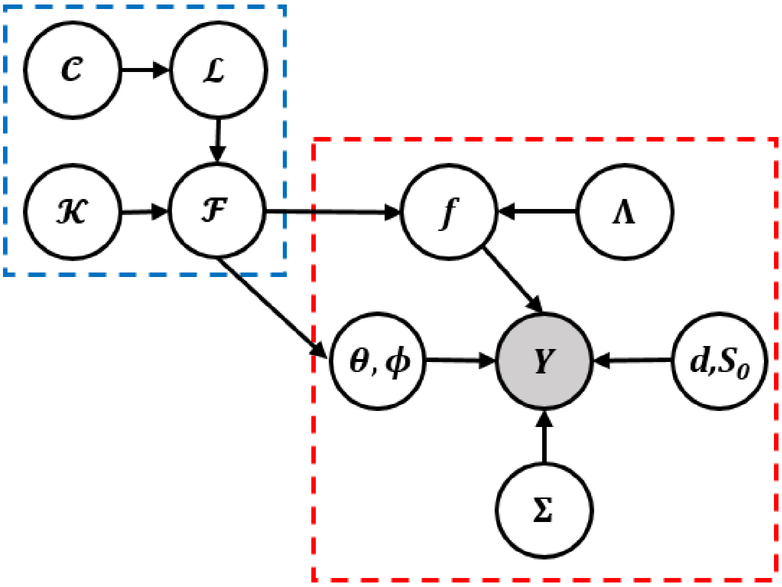

Figure 5: Bayesian framework, consists of parameters from the local partial volume model (red dashed box, with Y represents the measured data, S_0 is the non-diffusion-weighted signal, d is the diffusivity, f the contribution fraction, θ, ϕ are the fiber direction and orientation, and Σ and Λ represent the scale parameters), and the global parameters(blue dashed box, including the fiber connection $\mathcal{F}$, the existance of connection $\mathcal{C}$, the tract location $\mathcal{L}$, and the control points $\mathcal{K}$) (adapted from [17]).

This model admits that the parameters can influence each other, as well as information included in the data can back-propagate into the parameters. The set of global parameters consist of the fiber connections ($\mathcal{F}$), the priors on the existence of these connections ($\mathcal{C}$), the location of a tract within each ROI ($\mathcal{L}$), and the spline control points ($\mathcal{K}$). To provide better understanding an illustration of the global parameters is provided in Figure 6.

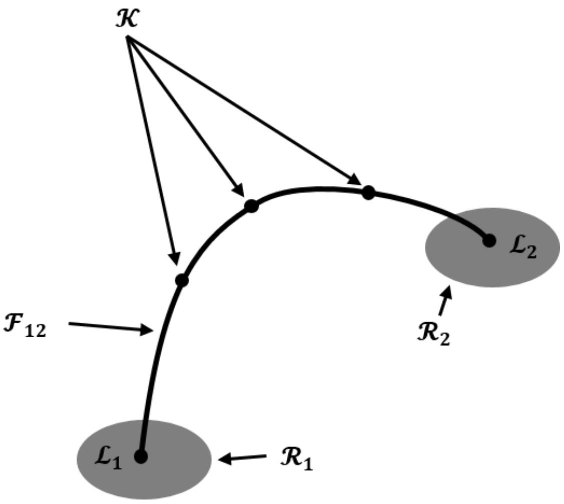

Figure 6: Representation of global parameters for the connection of regions $\mathcal{R}_1$ and $\mathcal{R}_2$ at the locations $\mathcal{L}_1$ and $\mathcal{L}_2$, by the fiber pathway $\mathcal{F}_{12}$, with $\mathcal{K}$ control points (adapted from [17]).

The set of N brain regions are represented by $\mathcal{R} = (\mathcal{R}_i)_{i=1:N}$. The existing connection of brain regions are expressed by the $N \times N$ matrix $\boldsymbol{C} = (c_{ij})$, where a prevailing connections is indicated by a c_{ij} value of 1 (and resp. by 0 if not connected). The random variable $\mathcal{L}_{ij}$ (resp. $\mathcal{L}_{ji}$) is a subset of $\mathcal{R}_i$ (resp. $\mathcal{R}_j$) which depict the location of pathway endings that are connected to $\mathcal{R}_j$ (resp. $\mathcal{R}_i$). The pathways connecting these subset regions are represented by the random variable $\mathcal{F}$. This variable could include values in the set of all possible 3D trajectories between two ROIs. Since this is not easily controllable, Catmull-Rom splines with a set of control points $\mathcal{K}$ were used. These are piece-wise cubic splines, and therefore easy to calculate as they do not have many parameters, and pass through all their control points in contrast to some B-spline curved. The posterior probability over all parameters, which summarizes the relationship of all parameters, is defined as:

$$\begin{aligned} p(\Omega|\boldsymbol{Y}) \propto\ & p(\boldsymbol{Y}|\boldsymbol{\Sigma}, \boldsymbol{d}, \boldsymbol{S}_0, \boldsymbol{f}, \boldsymbol{\theta}, \boldsymbol{\phi}) p(\boldsymbol{\Sigma}) p(\boldsymbol{d}) p(\boldsymbol{S}_0) \\ & p(\boldsymbol{\theta}, \boldsymbol{\phi}|\mathcal{F}) p(\boldsymbol{f}|\boldsymbol{\Lambda}, \mathcal{F}) p(\boldsymbol{\Lambda}) p(\mathcal{F}|\boldsymbol{C}) p(\boldsymbol{C}), \end{aligned} \tag{32}$$

where $\Omega = (\boldsymbol{\Sigma}, \boldsymbol{d}, \boldsymbol{S}_0, \boldsymbol{f}, \boldsymbol{\Lambda}, \boldsymbol{\theta}, \boldsymbol{\phi}, \boldsymbol{C}, \mathcal{F})$, and bold symbols and letters indicate vectors of values for all measurements. Furthermore, the unknown pathway $\mathcal{F}$ in any test subject is calculated from the DWI data $\boldsymbol{Y}$ by using the posterior probability distribution of $\mathcal{F}$ given $\boldsymbol{Y}$,

$$p(\mathcal{F}|\boldsymbol{Y}) \propto p(\boldsymbol{Y}|\mathcal{F})p(\mathcal{F}). \tag{33}$$

Differently to the approach introduced by Jbabdi et al. [17] which assumes equal prior probability for all possible pathways connecting two ROIs, TRACULA uses a prior defined as:

$$\mathrm{p}(\mathcal{F}) = p\left(\mathcal{F}\middle|\boldsymbol{A}, \{\boldsymbol{\mathcal{F}}_k\}_{k=1}^{N_t}, \{\boldsymbol{A}_K\}_{k=1}^{N_t}\right). \tag{34}$$

Here, $\boldsymbol{A}$ represents the anatomical segmentation map of the test subject, and $\boldsymbol{\mathcal{F}}_k$ and $\boldsymbol{A}_k$, $k = 1, \dots, N_t$, are the pathway of interest and the anatomical segmentation map for each training subject. The major WM pathways of interest were obtained by manual labeling of training subjects. This manual labeling was performed by an expert which drew at least two ROIs for each pathway that the pathway is known to traverse. The following pathways were labeled:

- Corticospinal tract (CST)
- Inferior longitudinal fasciculus (ILF)
- Uncinate fasciculus (UNC)
- Anterior thalamic radiation (ATR)
- Cingulum - cingulate gyrus bundle (CCG)
- Cingulum - angular bundle (CAB)
- Superior longitudinal fasciculus - parietal bundle (SLFP)
- Superior longitudinal fasciculus - temporal bundle (SLFT)
- Corpus callosum - forceps major (FMAJOR)
- Corpus callosum - forceps minor (FMINOR)

All pathways, except FMAJOR and FMINOR, were labeled on bilateral hemispheres which resulted in a total of 18 pathways for each subject. The anatomical segmentation maps $\boldsymbol{A}_k$ were acquired as described in Section 3.4.1 from the T_1-weighted image using FreeSurfer. The posterior distribution $p(\boldsymbol{\mathcal{F}}|\boldsymbol{Y})$ was estimated by using a Markov Chain Monte Carlo algorithm. All pathways for each test subject were modeled as cubic splines with a fixed number of control points. The number of control points (5) as well as the parameters for the Markov Chain Monte Carlo algorithm (200 “burn-in” iteration and 5000 main iteration) were set to default as defined by Yendiki et al. [16].

3.4.3 Postprocessing

Results from DTI analysis and automated tractography were visually verified for correct determination and reconstruction for every subject and entity.

3.5 Statistical analysis

All statistical analyses were performed using STATISTICA 12 (StatSoft, Tulsa, OK, USA). Mean values and standard deviations of diffusion properties (FA, MD, RD, and AD) of all WM tracts were extracted from the three iterations of the overall 7 multiresolution datasets. To infer to the computation stability, the extracted mean values and standard deviations of tract specific diffusion metric were then plotted over the number of applied diffusion gradient directions.

To relate the change and stability of determined diffusion values to age, mean values and standard deviation from normal healthy subjects were plotted over decades of age.

Parametric (Student t-test) or non-parametric tests (Mann-Whitney U test), if appropriate, were performed for comparing the two groups of ALS and healthy subjects, and to depict the effective possible clinical application of TRACULA. The Kolmogorov-Smirnov test and quantile-quantile plots were regarded to verify for normal distribution. A p-value less than 0.003 ($p < \frac{0.05}{18}$) was considered as statistically significant after Bonferroni correction to account for multiple comparison. Results were also indicated if they exceeded a lesser conservative significant threshold of 0.05.

4 Results

Overall, all steps of TRACULA were successfully implemented on the existing system and run without any errors. An exemplary three-dimensional reconstruction of all WM pathways with their corresponding description is presented in Figure 7. The here presented 3D structures provided by TRACULA, incorporate the volumetric probability distribution at 20% of its maximum value and from which further the tract related diffusion properties were extracted.

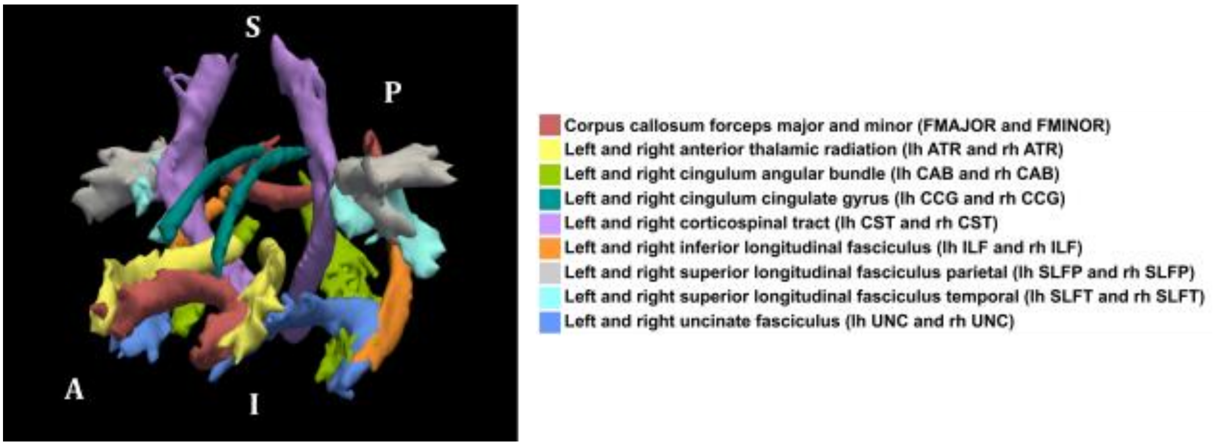

Figure 7: Three-dimensional representation of all 18 reconstructed WM tracts in relation to the anterior (A), posterior (P), superior (S), and inferior (I) directions.

4.1 Multiresolution dataset

Automated WM tract reconstruction passed successfully and in absence of any errors for all iterations of the 7 multiresolution datasets. Exemplary illustrations of TRACULA reconstruction depending on the number of diffusion gradients are shown in Figure 8 and Figure 9 for SS-EPI and readout segmented EPI datasets. In the case for low resolution SS-EPI datasets, the size of highly probable voxels which belonged to specific WM tracts decreased with increasing number of gradient directions. This effect however, was not observed for readout segmented EPI data. Even though there are slight differences in tract size for the different datasets.

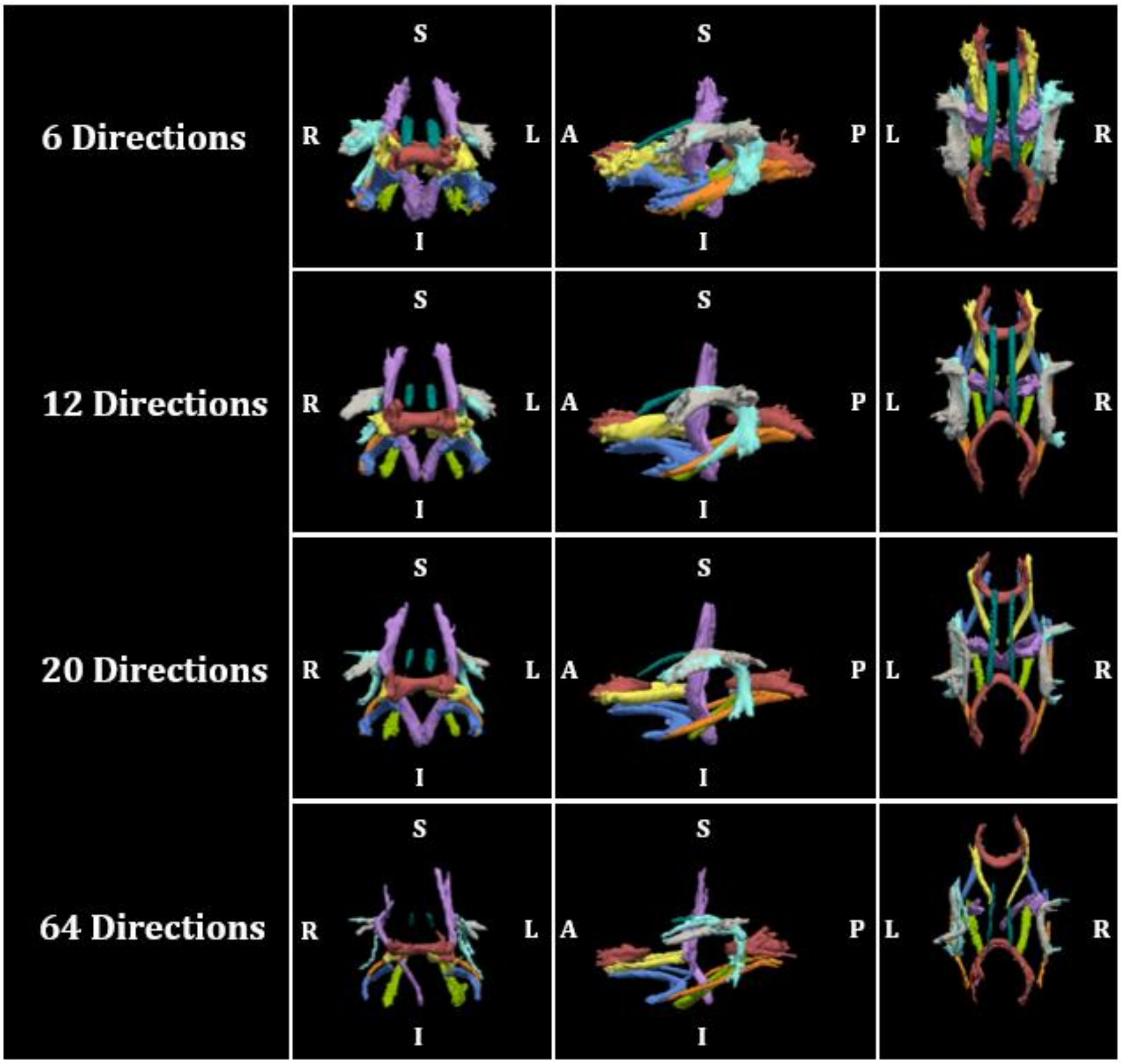

Figure 8: Reconstruction of WM tracts dependent on number of diffusion encoding gradients based on SS-EPI dataset. Here shown from left to right are front, side, and top view. Orientation of 3D tracts in relation to anterior (A), posterior (P), superior (S), inferior (I), left (L), and right (R) directions.

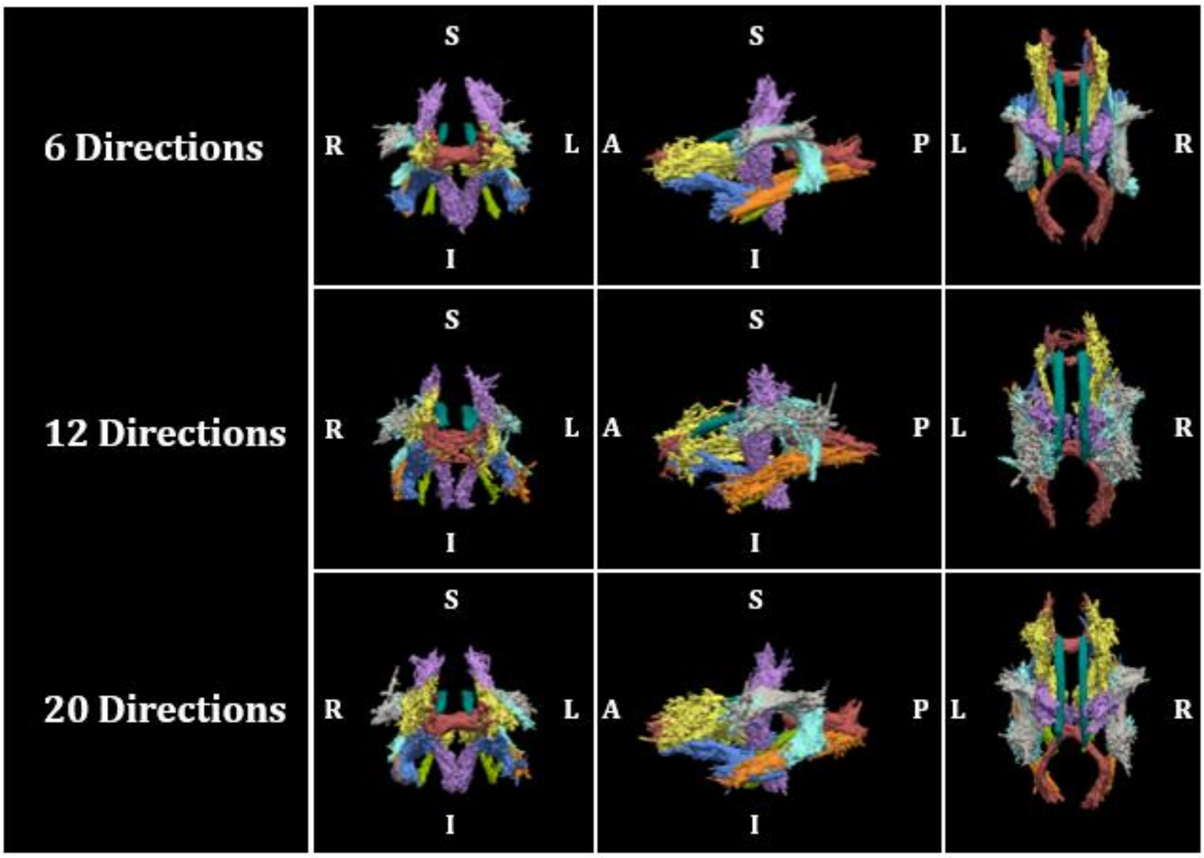

Figure 9: Reconstruction of WM tracts dependent on number of diffusion encoding gradients based on readout segmented EPI dataset. Here shown from left to right are front, side, and top view. Orientation of 3D tracts in relation to anterior (A), posterior (P), superior (S), inferior (I), left (L), and right (R) directions.

The change in mean values of extracted diffusion properties (FA, MD, RD, and AD) from all WM tracts over the number diffusion directions are shown in Figure 10-Figure 13 for low resolution SS-EPI datasets, and in Figure 14-Figure 17 for high-resolution readout segmented EPI datasets. Values of MD were roughly steady over the course of increasing number of diffusion direction both for SS-EPI and readout segmented EPI. Altough, some tracts (FMAJOR, right CAB, and bilateral CCG) showed a change in MD with increasing number of directions for low resolution data. However, an overall increase of RD, along with a decrease of FA (except for the corpus callosum - forceps major (FMAJOR) and minor (FMINOR)), was observed. Furthermore, while AD slightly decreased with more directions for high resolution data, low resolution datasets showed an increase as well as a decrease of AD for different fiber tracts. Moreover, overall extracted FA values were higher for high resolution datasets compared to SS-EPI datasets. A similar pattern was observed for MD, RD, and AD where extracted values were lower for readout segmented EPI datasets. Additionally, when comparing extracted DTI values from SS-EPI data and readout segmented data, it was found that for readout segmented EPI results their magnitude were similar across all tracts. Whereas DTI results from SS-EPI exhibited a larger range of extent across fiber tracts.

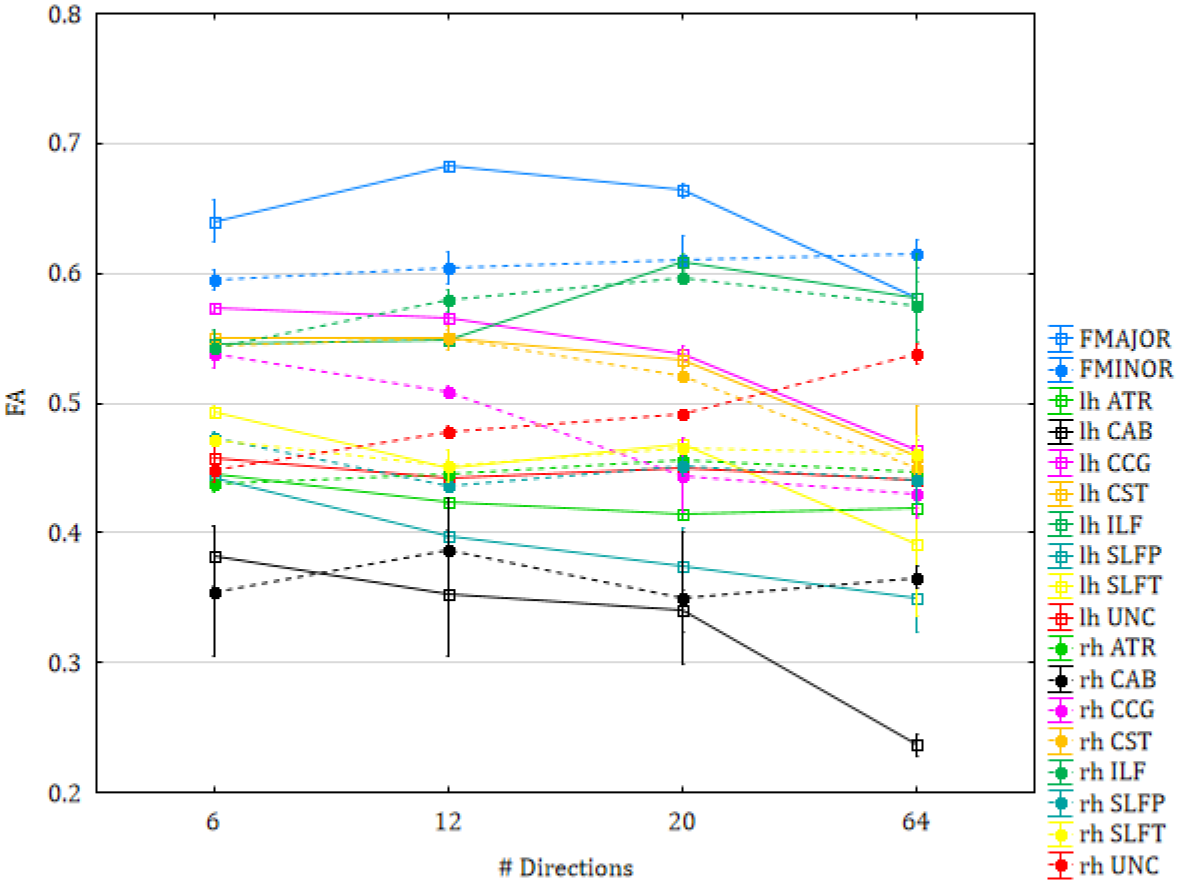

Figure 10: Change of FA in all reconstructed fiber tracts from SS-EPI dataset over the number of applied diffusion gradients (# Directions). Here shown are mean values and standard deviation for all applied number of directions. Corresponding structures are shown in the same color, but with different mean value markers and different line shape for left (lh) and right (rh) hemisphere or anterior and posterior orientation.

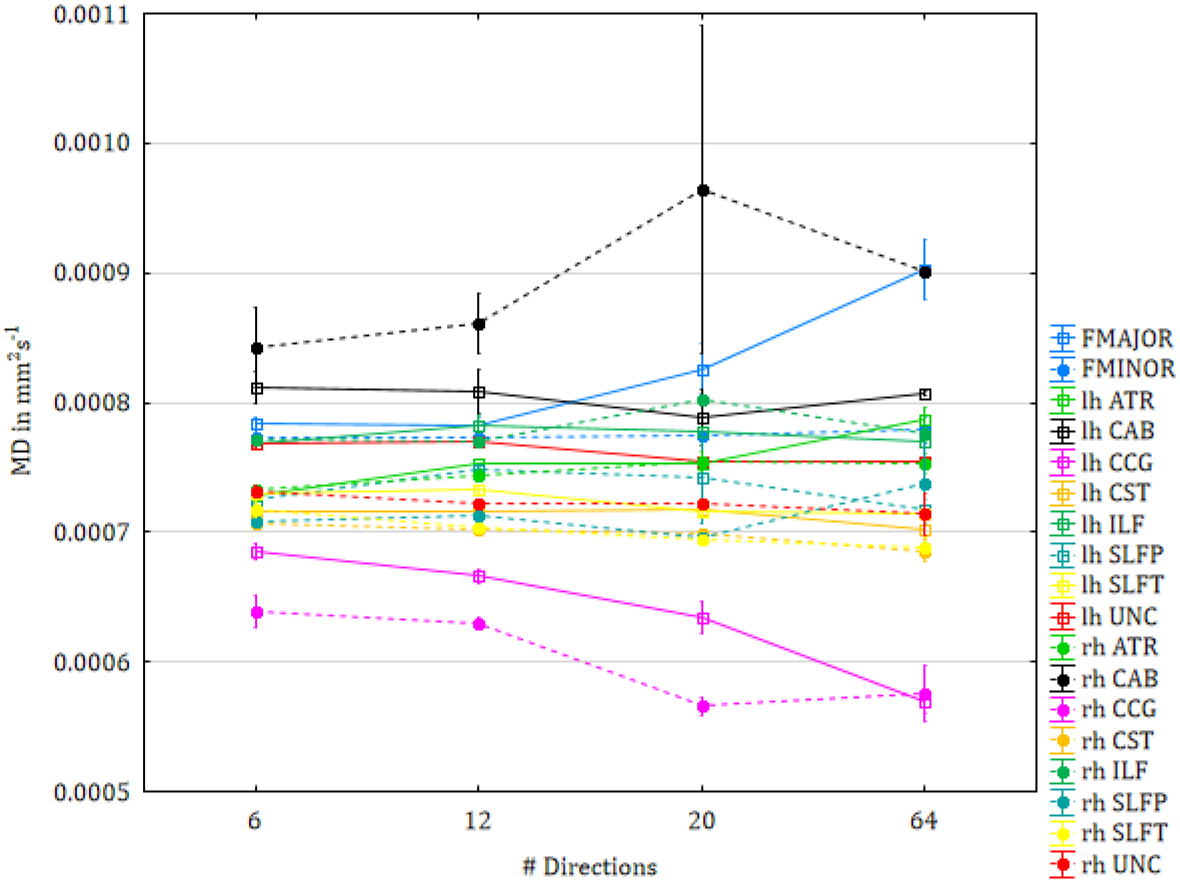

Figure 11: Change of MD in all reconstructed fiber tracts from SS-EPI dataset over the number of applied diffusion gradients (# Directions). Here shown are mean values and standard deviation for all applied number of directions. Corresponding structures are shown in the same color, but with different mean value markers and different line shape for left (lh) and right (rh) hemisphere or anterior and posterior orientation.

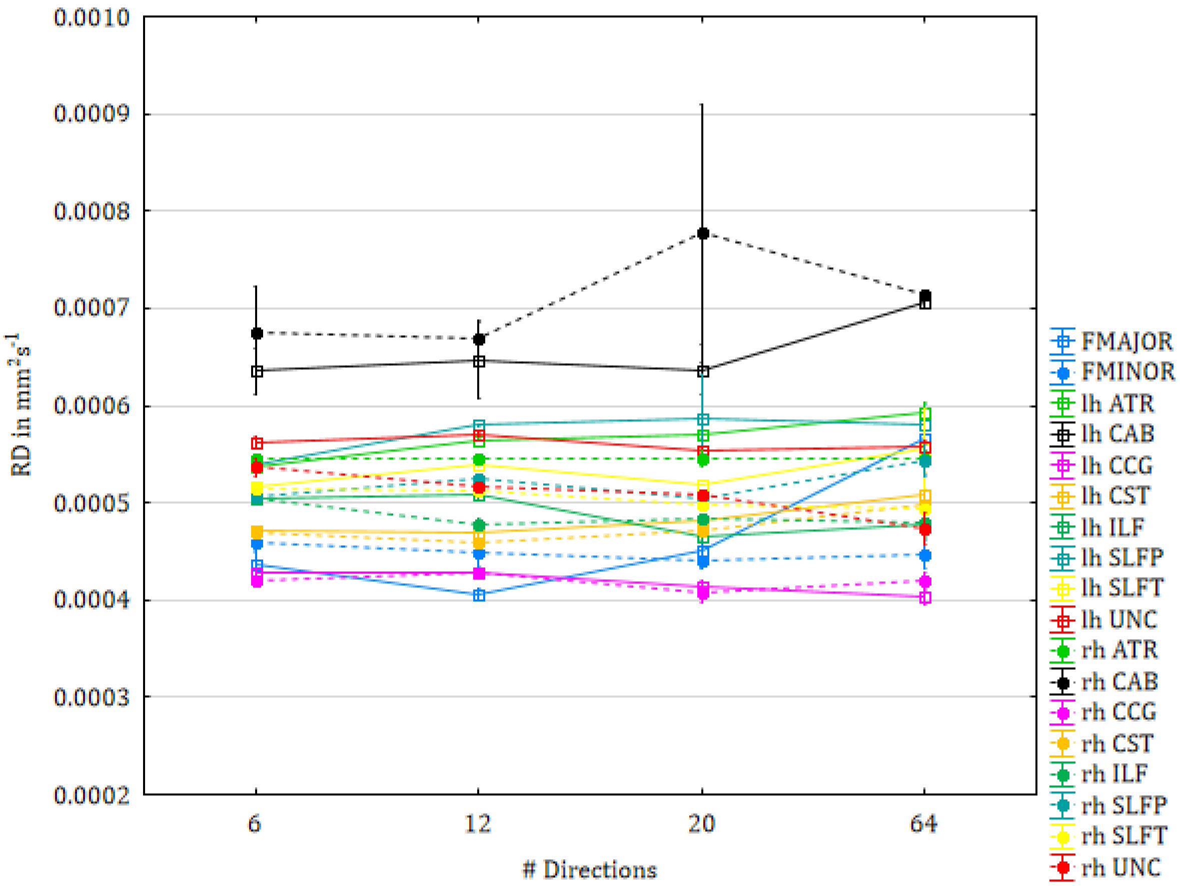

Figure 12: Change of RD in all reconstructed fiber tracts from SS-EPI dataset over the number of applied diffusion gradients (# Directions). Here shown are mean values and standard deviation for all applied number of directions. Corresponding structures are shown in the same color, but with different mean value markers and different line shape for left (lh) and right (rh) hemisphere or anterior and posterior orientation.

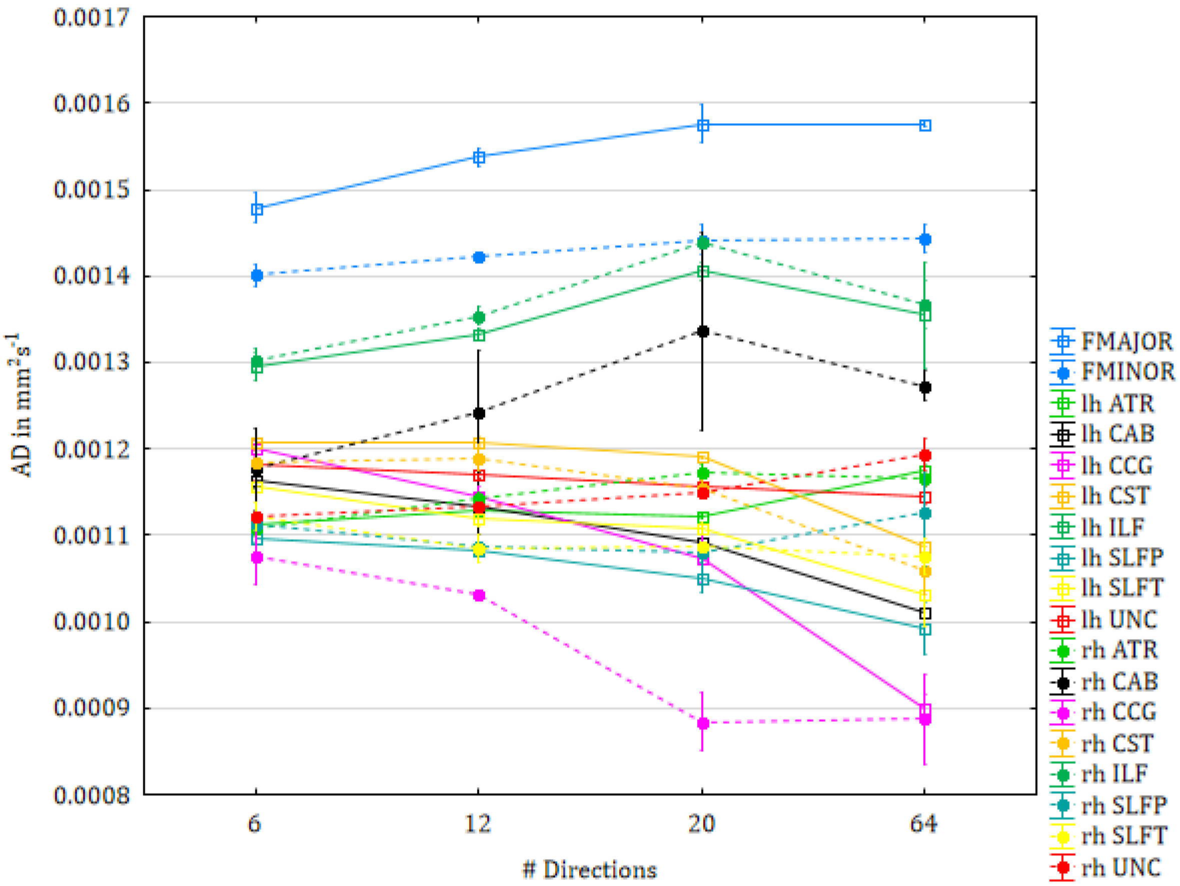

Figure 13: Change of AD in all reconstructed fiber tracts from SS-EPI dataset over the number of applied diffusion gradients (# Directions). Here shown are mean values and standard deviation for all applied number of directions. Corresponding structures are shown in the same color, but with different mean value markers and different line shape for left (lh) and right (rh) hemisphere or anterior and posterior orientation.

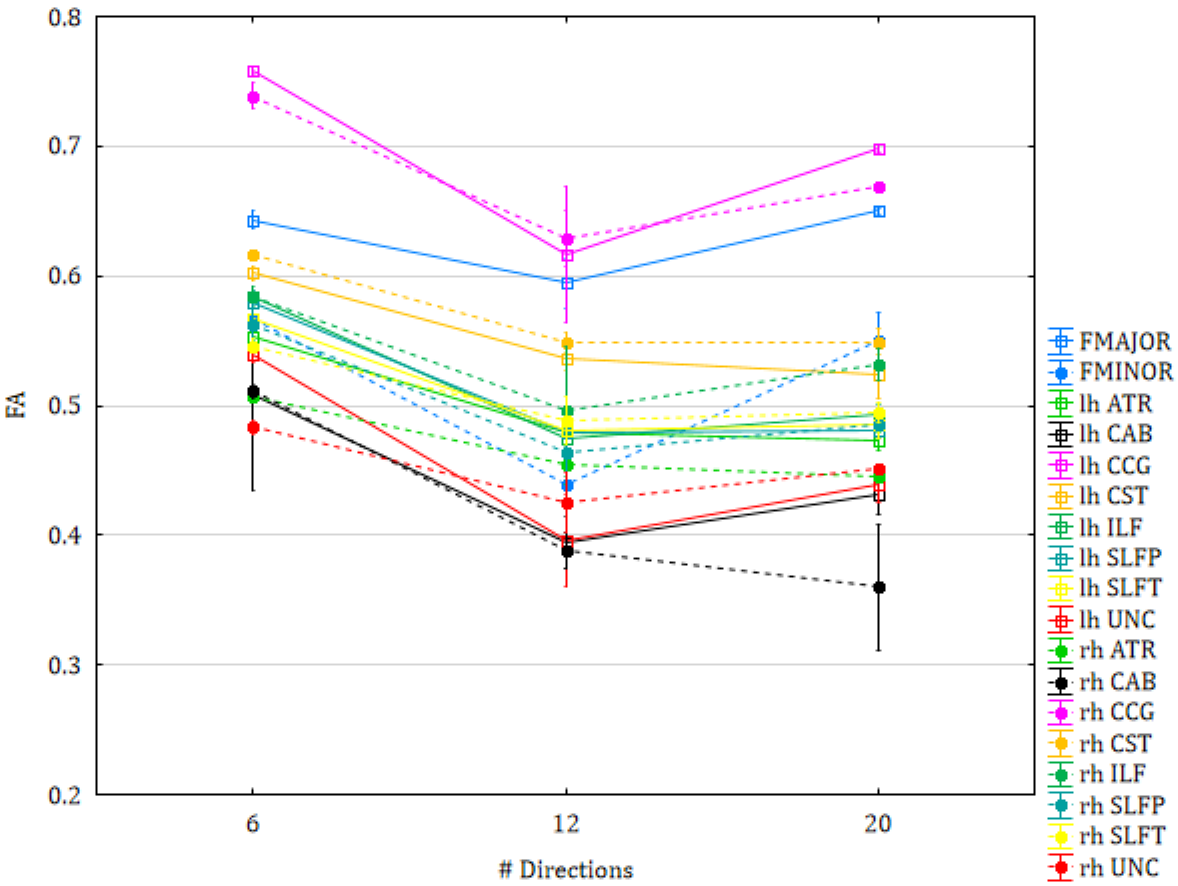

Figure 14: Change of FA in all reconstructed fiber tracts from readout segmented EPI dataset over the number of applied diffusion gradients (# Directions). Here shown are mean values and standard deviation for all applied number of directions. Corresponding structures are shown in the same color, but with different mean value markers and different line shape for left (lh) and right (rh) hemisphere or anterior and posterior orientation.

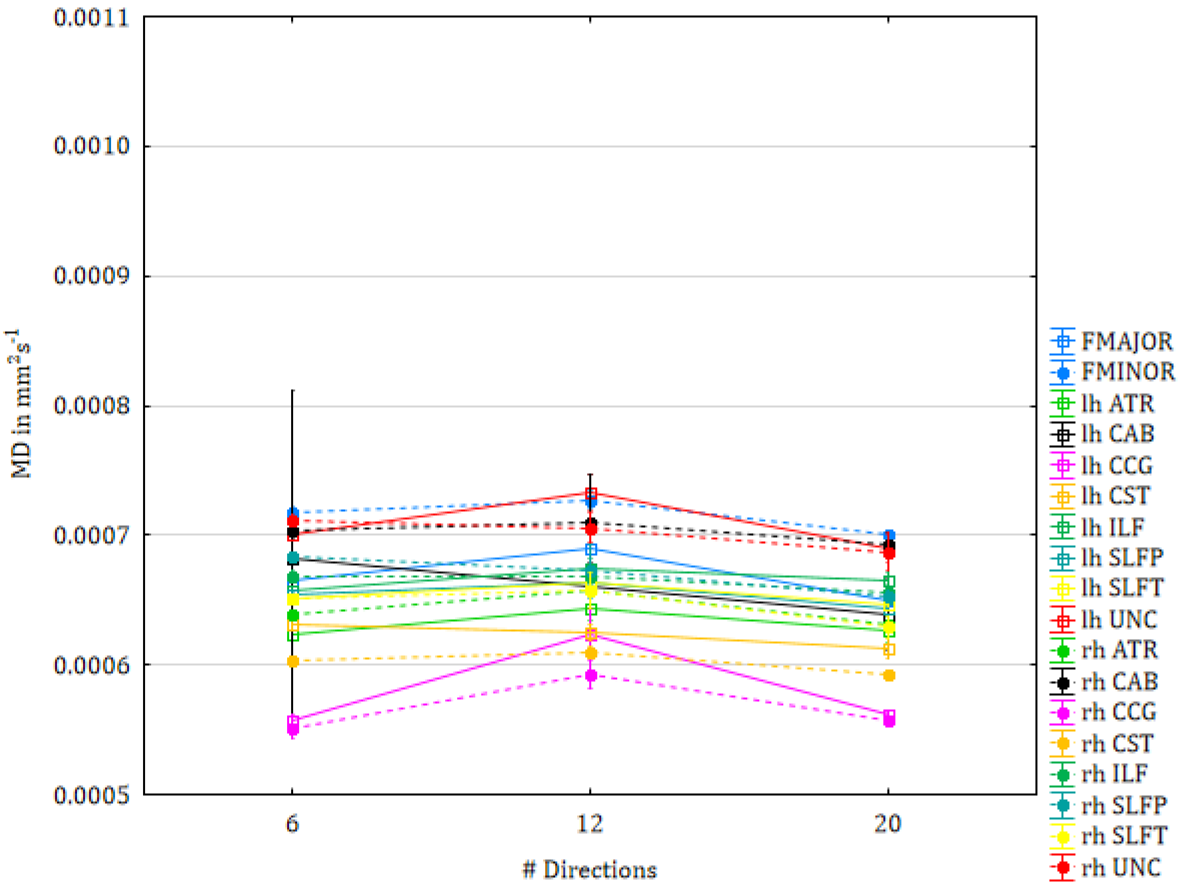

Figure 15: Change of MD in all reconstructed fiber tracts from readout segmented EPI dataset over the number of applied diffusion gradients (# Directions). Here shown are mean values and standard deviation for all applied number of directions. Corresponding structures are shown in the same color, but with different mean value markers and different line shape for left (lh) and right (rh) hemisphere or anterior and posterior orientation.

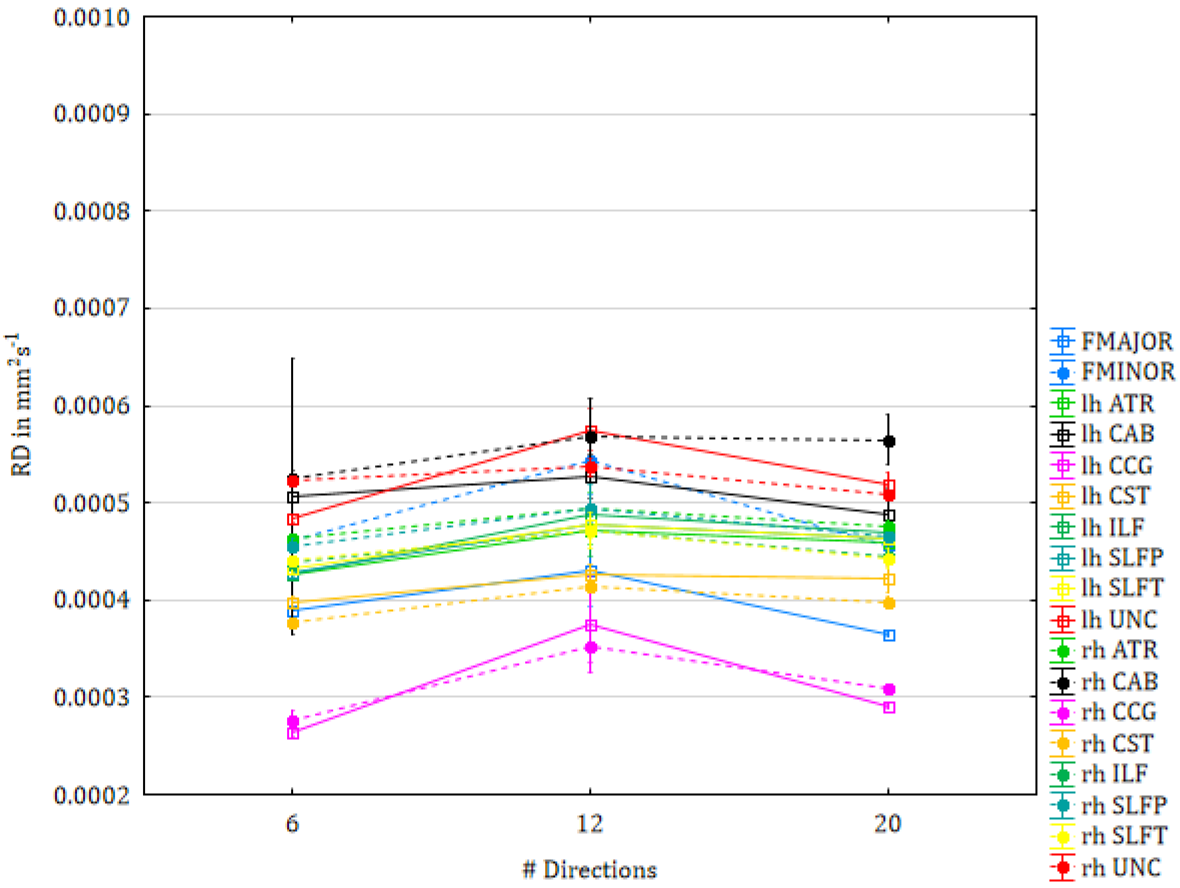

Figure 16: Change of RD in all reconstructed fiber tracts from readout segmented EPI dataset over the number of applied diffusion gradients (# Directions). Here shown are mean values and standard deviation for all applied number of directions. Corresponding structures are shown in the same color, but with different mean value markers and different line shape for left (lh) and right (rh) hemisphere or anterior and posterior orientation.

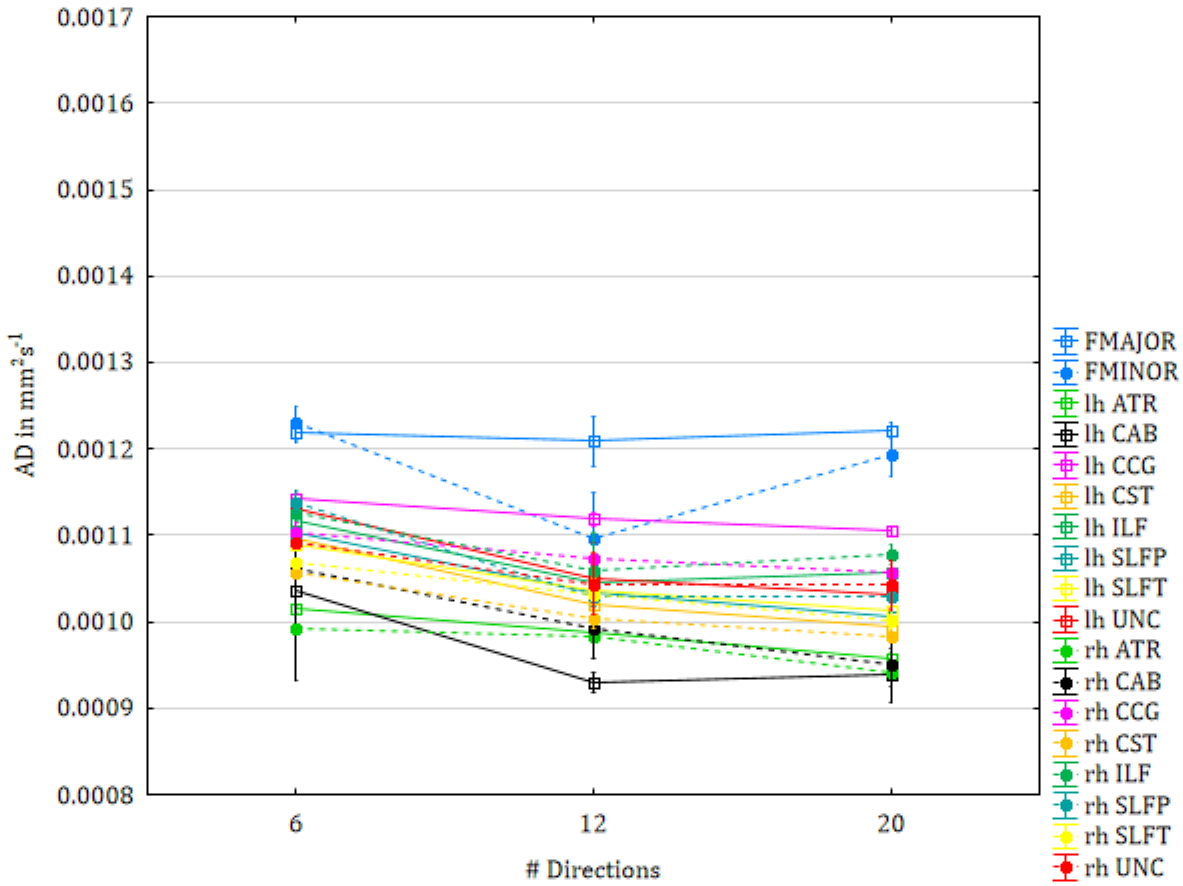

Figure 17: Change of AD in all reconstructed fiber tracts from readout segmented EPI dataset over the number of applied diffusion gradients (# Directions). Here shown are mean values and standard deviation for all applied number of directions. Corresponding structures are shown in the same color, but with different mean value markers and different line shape for left (lh) and right (rh) hemisphere or anterior and posterior orientation.

4.2 Normal Healthy Subjects

TRACULA performed automatic probabilistic tractography and extract DTI values in 205 of the initial 212 participants. However, in 10 cases of the fully processed datasets the reconstruction finished with at least one error. Which in turn resulted in an overall number of 195 successful reconstructed cases. Extracted mean DTI values from all WM tracts are plotted over age in Figure 18-Figure 21. A decrease of FA, along with a concomitant increase of MD, RD, and AD over age was detected for the majority of fiber tracts. Although, the observed extent of change was higher for MD and RD than for FA and AD.

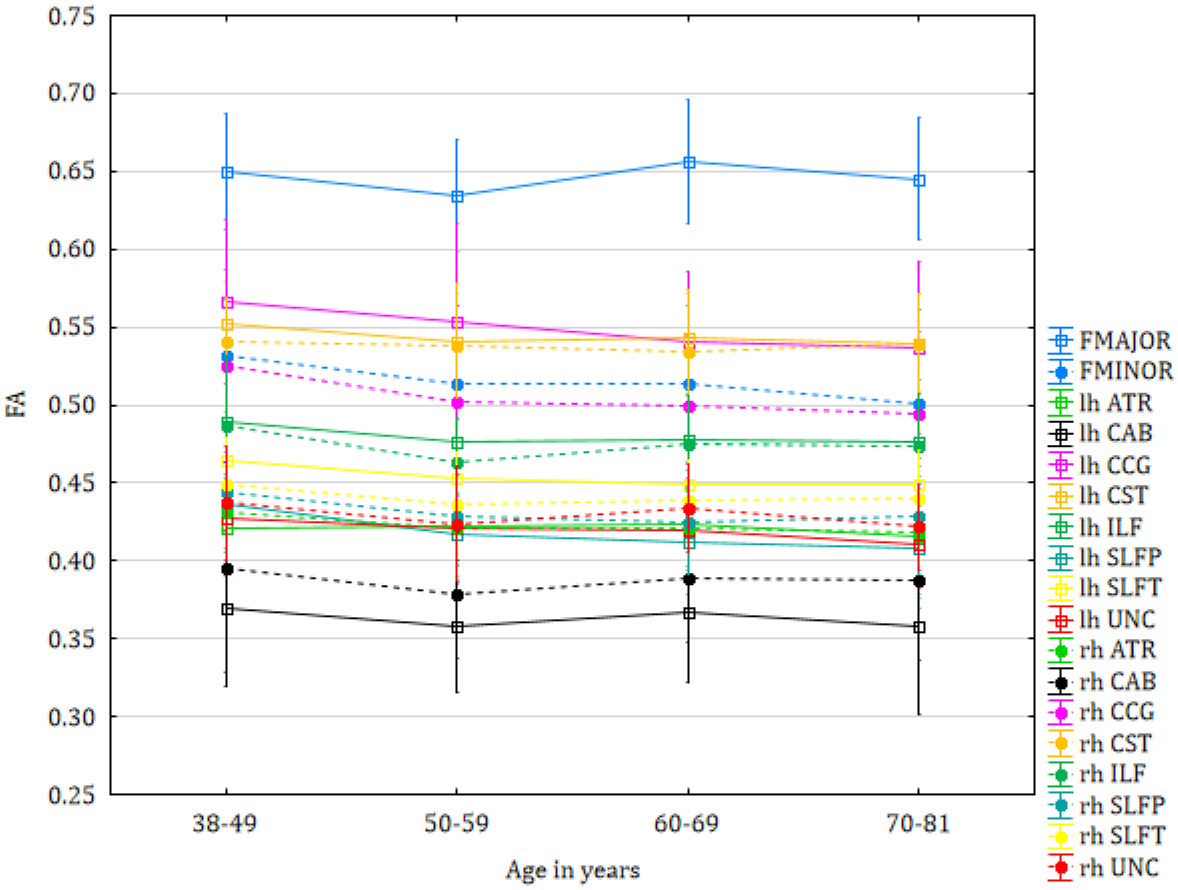

Figure 18: Change of FA in all reconstructed fiber tracts from normal healthy subjects over age. Here shown are mean values and standard deviation for every decade in age. Corresponding structures are shown in the same color, but with different mean value markers and different line shape for left (lh) and right (rh) hemisphere or anterior and posterior orientation.

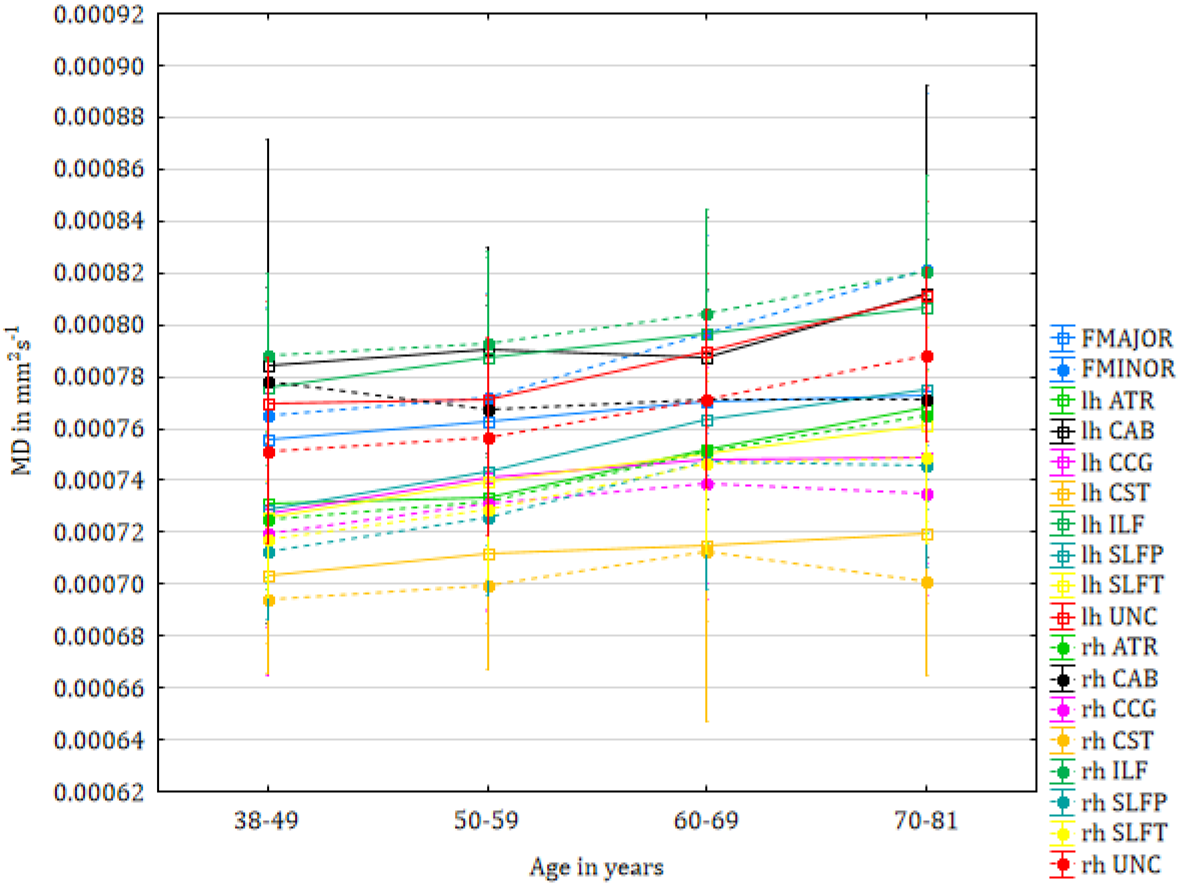

Figure 19: Change of MD in all reconstructed fiber tracts from normal healthy subjects over age. Here shown are mean values and standard deviation for every decade in age. Corresponding structures are shown in the same color, but with different mean value markers and different line shape for left (lh) and right (rh) hemisphere or anterior and posterior orientation.

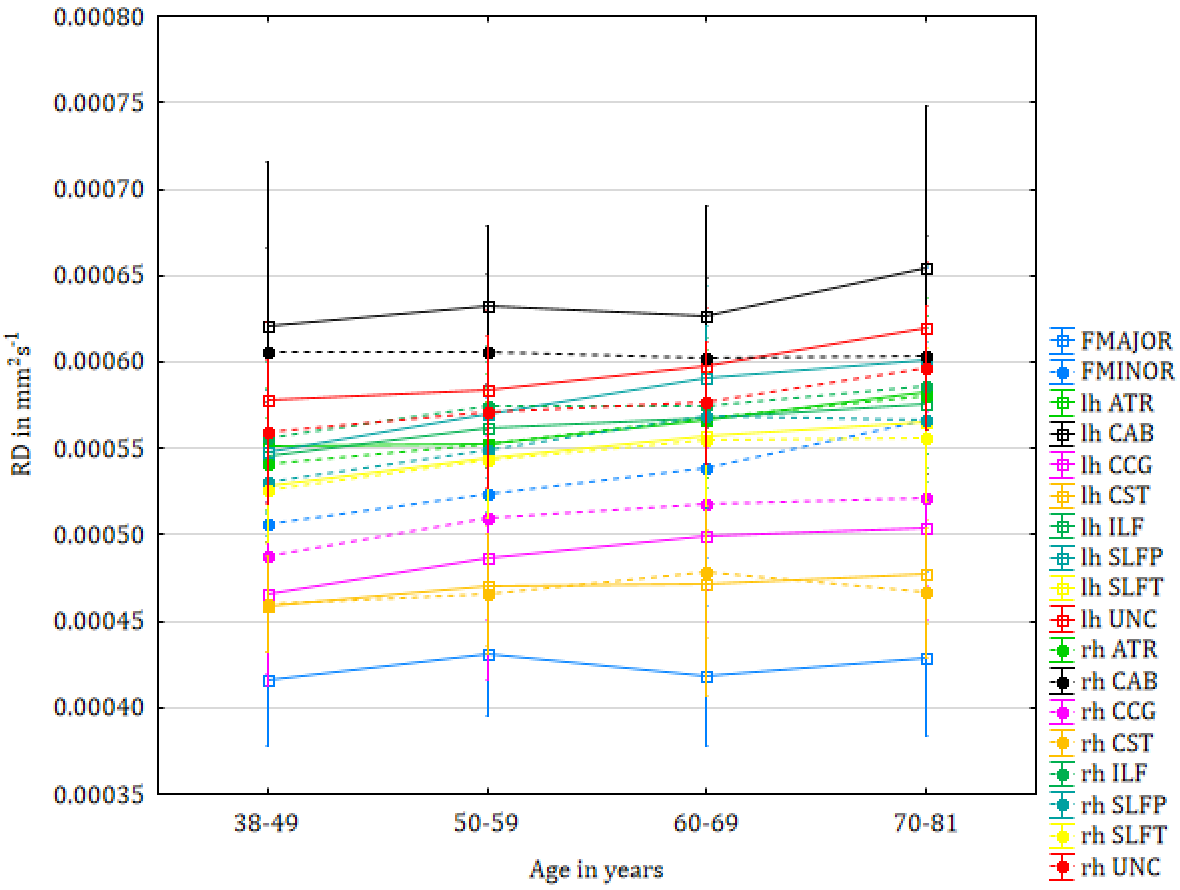

Figure 20: Change of RD in all reconstructed fiber tracts from normal healthy subjects over age. Here shown are mean values and standard deviation for every decade in age. Corresponding structures are shown in the same color, but with different mean value markers and different line shape for left (lh) and right (rh) hemisphere or anterior and posterior orientation.

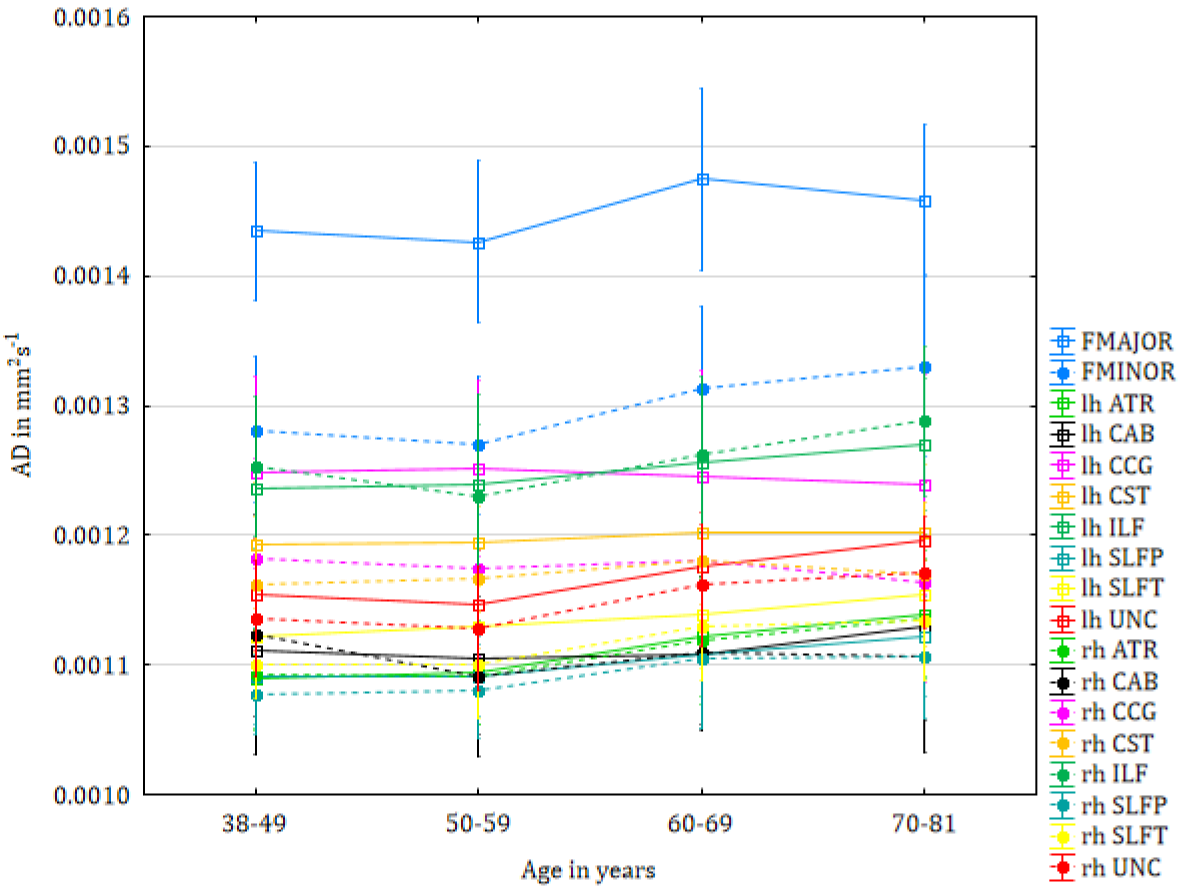

Figure 21: Change of AD in all reconstructed fiber tracts from normal healthy subjects over age. Here shown are mean values and standard deviation for every decade in age. Corresponding structures are shown in the same color, but with different mean value markers and different line shape for left (lh) and right (rh) hemisphere or anterior and posterior orientation.

4.3 ALS

It was possible to successfully run TRACULA in all ALS patients without any interruptions. ALS related changes of DTI quantities (FA, MD, RD, and AD) compared to healthy participants are listed in Table 1. Diffusion properties showed specific differences, which focused in the bilateral tracts of the CST. There, a significant increase of MD and RD, along with collateral decrease of FA was detected, while AD remained consistent. Furthermore, a minor significant decrease of FA was found for the left and right superior longitudinal fasciculus parietal (SLFP). In addition, a change of AD was only observed in the right uncinate fasciculus (UNC), which increased for ALS patients compared to normal subjects. All other tracts showed no abnormal changes of DTI parameters.

Table 1: Tract specific group analysis results of DTI properties in 18 WM tracts. Here provided are mean values ± standard deviation. Values for MD, RD, and AD are presented in $10^{-3}\ mm^2 s^{-1}$.

	FA		**MD**		**RD**		**AD**	
	ALS	HC	ALS	HC	ALS	HC	ALS	HC
N	27	195	27	195	27	195	27	195
FMAJOR	0.640±0.041	0.647±0.039	0.763±0.035	0.768±0.030	0.428±0.043	0.425±0.042	1.432±0.071	1.454±0.062
FMINOR	0.506±0.045	0.511±0.054	0.805±0.072	0.799±0.060	0.551±0.075	0.544±0.075	1.313±0.089	1.310±0.068
lh ATR	0.415±0.029	0.420±0.034	0.749±0.046	0.753±0.038	0.569±0.049	0.570±0.043	1.108±0.049	1.121±0.050
lh CAB	0.362±0.032	0.362±0.052	0.784±0.039	0.799±0.064	0.627±0.042	0.639±0.076	1.098±0.049	1.118±0.064
lh CCG	0.535±0.048	0.545±0.054	0.738±0.042	0.744±0.045	0.496±0.053	0.494±0.056	1.223±0.066	1.244±0.080
lh CST	0.504±0.033**	0.543±0.032**	0.733±0.032**	0.715±0.028**	0.509±0.036**	0.472±0.031**	1.180±0.049	1.199±0.052
lh ILF	0.471±0.040	0.479±0.037	0.794±0.039	0.797±0.037	0.570±0.046	0.566±0.042	1.244±0.057	1.257±0.055
lh SLFP	0.400±0.029*	0.416±0.037*	0.773±0.050	0.760±0.046	0.603±0.051	0.585±0.053	1.113±0.058	1.110±0.048
lh SLFT	0.441±0.032	0.453±0.033	0.762±0.044	0.750±0.036	0.569±0.048	0.554±0.042	1.147±0.051	1.142±0.042
lh UNC	0.410±0.022	0.417±0.031	0.793±0.049	0.794±0.040	0.606±0.047	0.603±0.043	1.166±0.057	1.177±0.048
rh ATR	0.410±0.030	0.422±0.034	0.751±0.041	0.751±0.042	0.573±0.044	0.567±0.048	1.107±0.049	1.118±0.049
rh CAB	0.371±0.037	0.389±0.052	0.770±0.053	0.772±0.063	0.613±0.060	0.604±0.072	1.085±0.053	1.108±0.074
rh CCG	0.496±0.062	0.502±0.055	0.729±0.043	0.732±0.044	0.513±0.060	0.513±0.056	1.161±0.074	1.172±0.074
rh CST	0.499±0.035**	0.539±0.032**	0.716±0.030†	0.702±0.043†	0.500±0.030††	0.468±0.045††	1.148±0.066	1.170±0.057
rh ILF	0.465±0.039	0.475±0.035	0.807±0.049	0.808±0.039	0.583±0.057	0.577±0.041	1.255±0.056	1.269±0.061
rh SLFP	0.413±0.034*	0.431±0.034*	0.744±0.047	0.738±0.041	0.571±0.051	0.558±0.046	1.089±0.059	1.097±0.047
rh SLFT	0.432±0.032	0.442±0.030	0.751±0.042	0.740±0.033	0.562±0.043	0.548±0.037	1.131±0.057	1.123±0.044
rh UNC	0.416±0.030	0.428±0.031	0.767±0.050	0.774±0.038	0.584±0.052	0.582±0.041	1.132±0.054*	1.157±0.048*

** $p < 0.003$ (after Bonferroni correction) using parametric testing, * p value < 0.05 using parametric testing,
†† $p < 0.003$ (after Bonferroni correction) using non-parametric testing, † $p < 0.05$ using non-parametric testing,
AD = axial diffusivity, RD = radial diffusivity, MD = mean diffusivity, FA = fractional anisotropy, N = number of subjects, ALS = amyotrophic lateral sclerosis, HC = healthy controls, FMAJOR = corpus callosum forceps major, FMINOR = corpus callosum forceps minor, ATR = anterior thalamic radiation, CAB = cingulum angular bundle, CCG = cingulum cingulate gyrus, CST = corticospinal tract, ILF = inferior longitudinal fasciculus, SLFP = superior longitudinal fasciculus parietal, SLFT = superior longitudinal fasciculus temporal, UNC = uncinate fasciculus, lh = left hemisphere, rh = right hemisphere

5 Discussion

This thesis demonstrates the successful implementation and execution of the automated global probabilistic tractography tool TRACULA. The here presented results regarding the stability with subject to the applied number of diffusion gradients and spatial resolution are in line with previous studies [60–62]. Moreover, it has been shown that TRACULA can be performed in a larger cohort. Where its reliability and coherent results are consistent with other work [63–65]. Finally, the potential of TRACULA being applied in clinical studies has been demonstrated while performing global probabilistic tractography and DTI in ALS. The results arisen from these analyses are in agreement with the literature [22, 48, 66]. Compared to tract-based spatial statistics (TBSS) [67], which is one of the most frequently used tools for DTI analysis. TRACULA is a subject based automated tractography method, where fiber tracts are more reliably determined, since tracts or their skeletons are not subject to misregistration [16]. Although, there exist other DTI and tractography software approaches [3, 68, 69], TRACULA has already been used in some studies and presented promising results [16, 48, 63, 70]. Furthermore, it utilizes additional well reviewed and reliable tools and methods, which are incorporated in the FreeSurfer and FSL software packages [16, 52, 53].

5.1 Software

All necessary software packages and software links to run TRACULA, were successfully implemented and established. Nevertheless, this was not as straight forward as one might think, and several adjustments or workarounds had to be established in combination with extensive discussions with the developers.

The user manual states that TRACULA accepts DICOM data as an input format. However, when first running the reconstruction with DICOM images, the algorithm stopped and displayed an error that it was not able to extract the b-factor data. Hence, the Siemens DICOM data were converted into the NIfTI format before handing them over to the DTI and tractography software.

This led to another problem. While converting from the DICOM to NIfTI format, the b-values and corresponding normalized gradient directions were extracted and saved in two separate row-ordered text-files. Since FSL tools only accept column-ordered files, these text-files had to be transformed to fulfill the requirements for FSL.

Since DWI data were transformed into the NIfTI format, TRACULA did not support multi subject processing anymore. Therefore, separate scripts had to be established which provide a workaround and performed data handling for multiple subjects at once.

Also, the choice of directory name had to be considered. Directory-names are not allowed to include the term “nii”, since TRACULA recognizes this term as a file extension. This would further lead to missing or not found files, which would excite multiple error-messages.

Even though English is the general working language in engineering- and computer-science, most operating systems in Austria are set to German as their system language. This introduced another issue, especially when working with different positional notation for numbers, where the different languages use different notations for decimal numbers. This resulted in the corruption of input numbers, and further to incorrect reconstructions and analyses. To resolve this problem, the system language had to be set to English en_US.UTF-8.

Model fitting was performed by FSL which fits the diffusion model to the DWI data. To do this TRACULA calls the command *bedpostx*, which starts a shell script. However, this was not the case in the first place. It was found that the issue had to do with the running 64-bit Ubuntu 12.04 operating system. For some reason, which is not completely clear yet, this called script had to be adjusted and converted into a bash script.

After completing tractography and DTI analysis, it was found while visually inspecting the results, that in some cases one or more WM tract distributions were represented as single 3D curve. line This resulted from a questionable initial guess for the pathway reconstruction, which could perhaps arise from poor image alignment. In cases with only one such single curve pathway, these corrupted tracts were reinitialized and reconstructed with a different initial guess. If this did not resolve the problem, and in cases with more than one defective tract, all steps, inputs, and outputs were extensively reviewed. Additionally, all identified issues were resolved if possible. Cases in which the problem persisted after rerunning TRACULA, or the cause could not have been identified, had been excluded from further investigations.

A newer version of TRACULA includes quality assessment of input data, so that issues like mentioned above can be identified in an early stage of processing. However, by the time of implementation the existing FreeSurfer software package on the existing server system did not support this version and therefore an older one was used. For future studies, the version of TRACULA should be updated since this would also enable the possibility of using more sophisticated DWI image correction methods against susceptibility- and eddy current-induced off-resonance fields, and analyses along the tracts.

Another downside was the limited number of tracts that could reconstructed by TRACULA in general. This number, however, should be extended in the future, which will increase the applicability of TRACULA overall. Nevertheless, the reconstructed tracts and their probability distributions which are available today, can not only be used to analyze DWI data but can also to generate ROIs which further allow for the tract-wise investigation of other MRI parameters.

5.2 Multiresolution dataset

Consistent with previous studies [60, 61, 71], a reduction of FA with increasing number of diffusion gradient directions was found. However, these results are in conflict with other reports [72, 73], which showed no change in FA with different number of diffusion directions. Regarding MD, the here presented results are in compliance with other research [61, 71], whereas an increase in MD was reported by others [60]. Furthermore, the observed increase in RD, along with a decrease in AD was also shown by others [61, 71].

When comparing results from high resolution readout segmented EPI data to low resolution SS-EPI data, it was found globally that FA was higher, and MD, RD, and AD were lower in high resolution datasets. These findings on FA, MD, and AD are consistent with another study [61]. However, not for RD. Furthermore, it was indicated that the extent of voxel anisotropy has an impact on extracted DTI values [74, 75]. Presented results originating from these features are concordant with earlier research [62, 76],but divergent to others [60].

The here reported DTI values are in the range of already published studies [60, 61, 71]. Nevertheless, they are not completely identical. These diversities might be caused by different sequence protocols, imaging parameters or field strength. Additionally, differences might also arise from the anisotropic voxel configuration and resolution, since these parameters can lead to different averaging of fiber orientation and partial volume effects, which can be well observed in Figure 8 [74, 75]. Therefore, to minimize the abovementioned issues, it is recommended to acquire volumes with high resolution isotropic resolution, and at least 20 diffusion encoding directions [60, 61, 74].

5.3 Normal Healthy Subjects

It has been shown that the DTI values on MD, RD, and AD increase over age, while values on FA concomitantly decrease. These results have been confirmed by earlier studies which also used TRACULA for tract-wise age-related analyses [63–65]. Furthermore, the here presented results are also in agreement with reports who used a different approach to study DTI values [77, 78]. Moreover, extracted DTI values were similar to values from the multiresolution dataset and compared studies [63, 77]. However, it was not possible to reconstruct and determine fiber tracts from all subject. This was due to missing high resolution structural images or volumetric labels, image artifacts, and misregistration (as described in Section 5.1). Nevertheless, it was possible to perform automatic probabilistic tractography in 195 of the initial 212 subject, which represents 92% of overall number. This indicates that TRACULA is a reliable tool, and further emphasizes its potential for clinical use.

5.4 ALS

The most consisting finding was the destruction of bilateral tracts of the CST. This is in agreement with pathology and the general observation in ALS [22, 48, 79]. Though, other studies failed to demonstrate degeneration for both or only one side of the CST [80, 81]. Furthermore, differences were found in complementary tracts of SLFP and for the right UNC. Unfortunately, a main limitation of this analysis comes from the different distributions of gender, age, and number of subject, which could affect the outcome of the here used analytical techniques. Nevertheless, these concerns can be neglected, since the ASPS cohort, which served as control group, holds a higher number of subjects and an overall higher age range. Therefore, it has been shown that TRACULA offers the potential to study pathological changes in ALS as well as other neurodegenerative diseases. Future investigations can also utilize the possibility of studying other MRI modalities in WM tracts reconstructed by TRACULA.

5.5 Statistical Analysis

In this work, only descriptive analysis were performed to investigate changes of DTI values over age and the number of diffusion encoding directions. Yet, many other studies use ANOVA analysis to characterize this change. However, this was a conscious choice based on the very high number of measures which would force the correction for multiple comparisons with Bonferroni correction and further impose an overly stringent significance level. Therefore, to investigate the extent of change further in-depth analysis are needed, which investigate only a limited amount of constraints.

In addition, unmatched groups were used to study ALS related microstructural tissue changes. These mismatches regarding gender, age, and number of subjects may prevent to illustrate the magnitude of change or even deliver misleading information. However, since the ASPS cohort, which served as control group, holds a higher number of subjects and an overall higher age, these considerations can be rejected. This decision was also supported by the results which are concurrent with literature.

5.6 Conclusion

In conclusion, this thesis presents the successful implementation and positive evaluation of TRACULA, a fully automated global probabilistic tractography tool. Since it allows for the automatic identification and reconstruction of 18 major WM tracts, and additionally determines all scalar parameters of the diffusion tensor, it speculates its further application in clinical use not only in ALS. The overall stability and reliability has been extensively investigated and verified over the course of this thesis. The here presented results are in conformity with the literature, which further emphasizes its applicability. However, it has been suggested that for future utilization a high number of diffusion encoding gradients, and high resolution imaging should be employed. Additional studies and technical developments are needed to strengthen this application and its daily clinical use.

References

[1] Le Bihan D, Iima M. Diffusion Magnetic Resonance Imaging: What Water Tells Us about Biological Tissues. PLOS Biol. 13(7): e1002203 (2015).

[2] Jones DK, Ed. Diffusion MRI: Theory, Methods, and Applications. Oxford University Press (2012).

[3] O'Donnell LJ, Pasternak O. Does diffusion MRI tell us anything about the white matter? An overview of methods and pitfalls. Schizophr Res. 161(1): 133–141 (2015).

[4] Le Bihan D, Johansen-Berg H. Diffusion MRI at 25: Exploring brain tissue structure and function. Neuroimage. 61(2): 324–341 (2012).

[5] Mori S, van Zijl PCM. Fiber tracking: principles and strategies - a technical review. NMR Biomed. 15(7–8): 468–480 (2002).

[6] Basser PJ, Mattiello J, LeBihan D. Estimation of the effective self-diffusion tensor from the NMR spin echo. J Magn Reson B. 103(3): 247–54 (1994).

[7] Pierpaoli C, Basser PJ. Toward a quantitative assessment of diffusion anisotropy. Magn Reson Med. 36(6): 893–906 (1996).

[8] Basser PJ, Pierpaoli C. Microstructural and physiological features of tissues elucidated by quantitative-diffusion-tensor MRI. J Magn Reson B. 111(3): 209–19 (1996).

[9] Basser PJ. New Histological and Physiological Stains Derived from Diffusion-Tensor MR Images. Ann N Y Acad Sci. 820(1 Imaging Brain): 123–138 (1997).

[10] Alexander AL, Hurley SA, Samsonov AA, Adluru N, Hosseinbor AP, Mossahebi P, *et al.* Characterization of Cerebral White Matter Properties Using Quantitative Magnetic Resonance Imaging Stains. Brain Connect. 1(6): 423–446 (2011).

[11] Alexander DC, Dyrby TB, Nilsson M, Zhang H. Imaging brain microstructure with diffusion MRI: Practicality and applications. NMR Biomed. (2017).

[12] Behrens TEJ, Woolrich MW, Jenkinson M, Johansen-Berg H, Nunes RG, Clare S, *et al.* Characterization and propagation of uncertainty in diffusion-weighted MR imaging. Magn Reson Med. 50(5): 1077–88 (2003).

[13] Tournier J-D, Mori S, Leemans A. Diffusion tensor imaging and beyond. Magn Reson Med. 65(6): 1532–1556 (2011).

[14] Jeurissen B, Descoteaux M, Mori S, Leemans A. Diffusion MRI fiber tractography of the brain. NMR Biomed. e3785 (2017).

[15] Mukherjee P, Berman JI, Chung SW, Hess CP, Henry RG. Diffusion tensor MR imaging and fiber tractography: theoretic underpinnings. AJNR Am J Neuroradiol. 29(4): 632–41 (2008).

[16] Yendiki A, Panneck P, Srinivasan P, Stevens A, Zöllei L, Augustinack J, *et al.* Automated probabilistic reconstruction of white-matter pathways in health and

disease using an atlas of the underlying anatomy. Front Neuroinform. 5(October): 23 (2011).

[17] Jbabdi S, Woolrich MW, Andersson JLR, Behrens TEJ. A Bayesian framework for global tractography. Neuroimage. 37(1): 116–29 (2007).

[18] Chekir A, Descoteaux M, Garyfallidis E, Cote M-A, Boumghar FO. A hybrid approach for optimal automatic segmentation of White Matter tracts in HARDI. In 2014 IEEE Conference on Biomedical Engineering and Sciences (IECBES). IEEE pp. 177–180 (2014).

[19] Yeatman JD, Dougherty RF, Myall NJ, Wandell BA, Feldman HM. Tract Profiles of White Matter Properties: Automating Fiber-Tract Quantification. PLoS One. 7(11): e49790 (2012).

[20] Schmidt R, Enzinger C, Ropele S, Schmidt H, Fazekas F. Progression of cerebral white matter lesions: 6-Year results of the Austrian Stroke Prevention Study. Lancet. 361(9374): 2046–2048 (2003).

[21] Schmidt R, Lechner H, Fazekas F, Niederkorn K, Reinhart B, Grieshofer P, *et al.* Assessment of cerebrovascular risk profiles in healthy persons: definition of research goals and the Austrian Stroke Prevention Study (ASPS). Neuroepidemiology. 13(6): 308–13 (1994).

[22] Borsodi F, Culea V, Langkammer C, Khalil M, Pirpamer L, Quasthoff S, *et al.* Multimodal assessment of white matter tracts in amyotrophic lateral sclerosis. PLoS One. 12(6): e0178371 (2017).

[23] Minati L, Węglarz WP. Physical foundations, models, and methods of diffusion magnetic resonance imaging of the brain: A review. Concepts Magn Reson Part A. 30A(5): 278–307 (2007).

[24] Kiselev VG. Fundamentals of diffusion MRI physics. NMR Biomed. 30(3): e3602 (2017).

[25] Tofts P, Ed. Quantitative MRI of the Brain. John Wiley & Sons, Ltd: Chichester, UK (2003).

[26] Johansen-Berg H, Behrens TEJ. Diffusion MRI : from quantitative measurement to in-vivo neuroanatomy. Elsevier Science (2014).

[27] Callaghan PT. Principles of nuclear magnetic resonance microscopy. Clarendon Press (1993).

[28] Kärger J, Heink W. The propagator representation of molecular transport in microporous crystallites. J Magn Reson. 51(1): 1–7 (1983).

[29] Koay CG, Özarslan E. Conceptual foundations of diffusion in magnetic resonance. Concepts Magn Reson Part A. 42(4): 116–129 (2013).

[30] Price WS. Pulsed-field gradient nuclear magnetic resonance as a tool for studying translational diffusion: Part 1. Basic theory. Concepts Magn Reson. 9(5): 299–336 (1997).

[31] Stejskal EO, Tanner JE. Spin Diffusion Measurements: Spin Echoes in the Presence of a Time-Dependent Field Gradient. J Chem Phys. 42(1): 288–292 (1965).

[32] Turner R, Le Bihan D, Maier J, Vavrek R, Hedges LK, Pekar J. Echo-planar imaging of intravoxel incoherent motion. Radiology. 177(2): 407–14 (1990).

[33] Holdsworth SJ, Skare S, Newbould RD, Guzmann R, Blevins NH, Bammer R. Readout-segmented EPI for rapid high resolution diffusion imaging at 3T. Eur J Radiol. 65(1): 36–46 (2008).

[34] Porter DA, Heidemann RM. High resolution diffusion-weighted imaging using readout-segmented echo-planar imaging, parallel imaging and a two-dimensional navigator-based reacquisition. Magn Reson Med. 62(2): 468–475 (2009).

[35] Le Bihan D, Turner R, Moonen CTW, Pekar J. Imaging of diffusion and microcirculation with gradient sensitization: Design, strategy, and significance. J Magn Reson Imaging. 1(1): 7–28 (1991).

[36] Le Bihan D, Breton E, Lallemand D, Grenier P, Cabanis E, Laval-Jeantet M. MR imaging of intravoxel incoherent motions: application to diffusion and perfusion in neurologic disorders. Radiology. 161(2): 401–7 (1986).

[37] Schaefer PW, Grant PE, Gonzalez RG. Diffusion-weighted MR Imaging of the Brain. Radiology. 217(2): 331–345 (2000).

[38] Basser PJ, Mattiello J, LeBihan D. MR diffusion tensor spectroscopy and imaging. Biophys J. 66(1): 259–67 (1994).

[39] Kingsley PB. Introduction to diffusion tensor imaging mathematics: Part III. Tensor calculation, noise, simulations, and optimization. Concepts Magn Reson Part A. 28A(2): 155–179 (2006).

[40] Hasan KM, Narayana PA. Computation of the fractional anisotropy and mean diffusivity maps without tensor decoding and diagonalization: Theoretical analysis and validation. Magn Reson Med. 50(3): 589–598 (2003).

[41] Novikov DS, Fieremans E, Jespersen SN, Kiselev VG. Quantifying brain microstructure with diffusion MRI: Theory and parameter estimation. ArXiv. 1612.02059 (2016).

[42] Caruyer E, Lenglet C, Sapiro G, Deriche R. Design of multishell sampling schemes with uniform coverage in diffusion MRI. Magn Reson Med. 69(6): 1534–1540 (2013).

[43] Basser PJ, Pajevic S, Pierpaoli C, Duda J, Aldroubi A. In vivo fiber tractography using DT-MRI data. Magn Reson Med. 44(4): 625–632 (2000).

[44] Hopewell JC, Clarke R. Emerging Risk Factors for Stroke. Stroke. 47(6): 1673–1678 (2016).

[45] Kiernan MC, Vucic S, Cheah BC, Turner MR, Eisen A, Hardiman O, *et al.* Amyotrophic lateral sclerosis. Lancet. 377(9769): 942–55 (2011).

[46] Hardiman O, van den Berg LH, Kiernan MC. Clinical diagnosis and management of amyotrophic lateral sclerosis. Nat Rev Neurol. 7(11): 639–49 (2011).

[47] Brooks BR, Miller RG, Swash M, Munsat TL. El Escorial revisited: revised criteria for the diagnosis of amyotrophic lateral sclerosis. Amyotroph Lateral Scler Other Motor Neuron Disord. 1(5): 293–299 (2000).

[48] Sarica A, Cerasa A, Vasta R, Perrotta P, Valentino P, Mangone G, *et al.* Tractography in amyotrophic lateral sclerosis using a novel probabilistic tool: a study with tract-based reconstruction compared to voxel-based approach. J Neurosci Methods. 224: 79–87 (2014).

[49] Wang S, Melhem ER, Poptani H, Woo JH. Neuroimaging in Amyotrophic Lateral Sclerosis. Neurotherapeutics. 8(1): 63–71 (2011).

[50] Rocha AJ Da, Maia Júnior ACM. Is magnetic resonance imaging a plausible biomarker for upper motor neuron degeneration in amyotrophic lateral sclerosis/primary lateral sclerosis or merely a useful paraclinical tool to exclude mimic syndromes? A critical review of imaging applicability . Arq Neuropsiquiatr. 70(February 2012): 532–539 (2012).

[51] Cedarbaum JM, Stambler N, Malta E, Fuller C, Hilt D, Thurmond B, *et al.* The ALSFRS-R: a revised ALS functional rating scale that incorporates assessments of respiratory function. J Neurol Sci. 169(1–2): 13–21 (1999).

[52] Fischl B. FreeSurfer. Neuroimage. 62(2): 774–81 (2012).

[53] Jenkinson M, Beckmann CF, Behrens TEJ, Woolrich MW, Smith SM. FSL. Neuroimage. 62(2): 782–90 (2012).

[54] Li X, Morgan PS, Ashburner J, Smith J, Rorden C. The first step for neuroimaging data analysis: DICOM to NIfTI conversion. J Neurosci Methods. 264: 47–56 (2016).

[55] Dale AM, Fischl B, Sereno MI. Cortical Surface-Based Analysis: I. Segmentation and Surface Reconstruction. Neuroimage. 9(2): 179–194 (1999).

[56] Fischl B, Salat DH, Busa E, Albert M, Dieterich M, Haselgrove C, *et al.* Whole Brain Segmentation: Automated Labeling of Neuroanatomical Structures in the Human Brain. Neuron. 33(3): 341–355 (2002).

[57] Fischl B, van der Kouwe A, Destrieux C, Halgren E, Ségonne F, Salat DH, *et al.* Automatically Parcellating the Human Cerebral Cortex. Cereb Cortex. 14(1): 11–22 (2004).

[58] Kingsley PB. Introduction to diffusion tensor imaging mathematics: Part II. Anisotropy, diffusion-weighting factors, and gradient encoding schemes. Concepts Magn Reson Part A. 28A(2): 123–154 (2006).

[59] Behrens TEJ, Berg HJ, Jbabdi S, Rushworth MFS, Woolrich MW. Probabilistic diffusion tractography with multiple fibre orientations: What can we gain? Neuroimage. 34(1): 144–55 (2007).

[60] Lebel C, Benner T, Beaulieu C. Six is enough? Comparison of diffusion parameters measured using six or more diffusion-encoding gradient directions with deterministic tractography. Magn Reson Med. 68(2): 474–483 (2012).

[61] Barrio-Arranz G, de Luis-García R, Tristán-Vega A, Martín-Fernández M, Aja-Fernández S. Impact of MR Acquisition Parameters on DTI Scalar Indexes: A Tractography Based Approach. PLoS One. 10(10): e0137905 (2015).

[62] Tudela R, Muñoz-Moreno E, López-Gil X, Soria G. Effects of Orientation and Anisometry of Magnetic Resonance Imaging Acquisitions on Diffusion Tensor

Imaging and Structural Connectomes. PLoS One. 12(1): e0170703 (2017).

[63] Fjell AM, Sneve MH, Grydeland H, Storsve AB, Amlien IK, Yendiki A, *et al.* Relationship between structural and functional connectivity change across the adult lifespan: A longitudinal investigation. Hum Brain Mapp. 38(1): 561–573 (2017).

[64] Li P, Tsapanou A, Qolamreza RR, Gazes Y. White matter integrity mediates decline in age-related inhibitory control. Behav Brain Res. 339: 249–254 (2018).

[65] Gazes Y, Bowman FD, Razlighi QR, O'Shea D, Stern Y, Habeck C. White matter tract covariance patterns predict age-declining cognitive abilities. Neuroimage. 125: 53–60 (2016).

[66] Westeneng H-J, Walhout R, Straathof M, Schmidt R, Hendrikse J, Veldink JH, *et al.* Widespread structural brain involvement in ALS is not limited to the C9orf72 repeat expansion. J Neurol Neurosurg Psychiatry. 87(12): 1354–1360 (2016).

[67] Smith SM, Jenkinson M, Johansen-Berg H, Rueckert D, Nichols TE, Mackay CE, *et al.* Tract-based spatial statistics: Voxelwise analysis of multi-subject diffusion data. Neuroimage. 31(4): 1487–1505 (2006).

[68] Hasan KM, Walimuni IS, Abid H, Hahn KR. A review of diffusion tensor magnetic resonance imaging computational methods and software tools. Comput Biol Med. 41(12): 1062–1072 (2011).

[69] Soares JM, Marques P, Alves V, Sousa N. A hitchhiker's guide to diffusion tensor imaging. Front Neurosci. 7: 31 (2013).

[70] Yendiki A, Reuter M, Wilkens P, Rosas HD, Fischl B. Joint reconstruction of white-matter pathways from longitudinal diffusion MRI data with anatomical priors. Neuroimage. 127: 277–286 (2016).

[71] Liu X, Yang Y, Sun J, Yu G, Xu J, Niu C, *et al.* Reproducibility of diffusion tensor imaging in normal subjects: an evaluation of different gradient sampling schemes and registration algorithm. Neuroradiology. 56(6): 497–510 (2014).

[72] Ni H, Kavcic V, Zhu T, Ekholm S, Zhong J. Effects of Number of Diffusion Gradient Directions on Derived Diffusion Tensor Imaging Indices in Human Brain. Am J Neuroradiol. 25(9): 1569–1574 (2006).

[73] Zhang N, Deng Z, Yin X, Liu X, Zheng H. Effect of Different Number of Diffusion Gradients on Dispersion Degree of FA Values and Its SNR. In 2010 4th International Conference on Bioinformatics and Biomedical Engineering. IEEE pp. 1–4 (2010).

[74] Jones DK, Knösche TR, Turner R. White matter integrity, fiber count, and other fallacies: The do's and don'ts of diffusion MRI. Neuroimage. 73: 239–254 (2013).

[75] Mukherjee P, Chung SW, Berman JI, Hess CP, Henry RG. Diffusion tensor MR imaging and fiber tractography: technical considerations. AJNR Am J Neuroradiol. 29(5): 843–52 (2008).

[76] Oouchi H, Yamada K, Sakai K, Kizu O, Kubota T, Ito H, *et al.* Diffusion Anisotropy Measurement of Brain White Matter Is Affected by Voxel Size: Underestimation

Occurs in Areas with Crossing Fibers. Am J Neuroradiol. 28(6) (2007).

[77] Giorgio A, Santelli L, Tomassini V, Bosnell R, Smith S, De Stefano N, *et al.* Age-related changes in grey and white matter structure throughout adulthood. Neuroimage. 51(3): 943–51 (2010).

[78] Salat DH, Tuch DS, Greve DN, van der Kouwe AJW, Hevelone ND, Zaleta AK, *et al.* Age-related alterations in white matter microstructure measured by diffusion tensor imaging. Neurobiol Aging. 26(8): 1215–1227 (2005).

[79] Sage CA, Peeters RR, Görner A, Robberecht W, Sunaert S. Quantitative diffusion tensor imaging in amyotrophic lateral sclerosis. Neuroimage. 34(2): 486–99 (2007).

[80] Verstraete E, Polders DL, Mandl RCW, Van Den Heuvel MP, Veldink JH, Luijten P, *et al.* Multimodal tract-based analysis in ALS patients at 7T: a specific white matter profile? Amyotroph Lateral Scler Frontotemporal Degener. 15(1–2): 84–92 (2014).

[81] Langkammer C, Enzinger C, Quasthoff S, Grafenauer P, Soellinger M, Fazekas F, *et al.* Mapping of iron deposition in conjunction with assessment of nerve fiber tract integrity in amyotrophic lateral sclerosis. J Magn Reson Imaging. 31(6): 1339–45 (2010).